Modeling heterogeneity of Triple-Negative Breast Cancer highlights potency of WEE1 and BCL-XL targeting

Fabienne Lamballe[1,8,10], Fahmida Ahmad[1,8], Yaron Vinik[2], Olivier Castellanet[1], Fabrice Daian[1], Anna-Katharina Müller[2], Ulrike A. Köhler[2], Anne-Laure Bailly[3], Emmanuelle Josselin[4], Rémy Castellano[4], Christelle Cayrou[3], Emmanuelle Charafe-Jauffret[5], Gordon B. Mills[6], Vincent Géli[3], Jean-Paul Borg[3,7], Sima Lev[2,9], Flavio Maina[1,9,10]

[1] Aix Marseille Univ, CNRS, Developmental Biology Institute of Marseille (IBDM), Turing Center for Living Systems, Parc Scientifique de Luminy, Marseille (France)

[2] Weizmann Institute of Science, Department of Molecular Cell Biology, Rehovot (Israel)

[3] Aix Marseille Univ, Centre de Recherche en Cancérologie de Marseille (CRCM), Equipes labellisées Ligue 'Cell polarity, cell signaling and cancer' and 'Telomere and Chromatin', Inserm, CNRS, Institut Paoli-Calmettes, Marseille (France)

[4] Aix Marseille Univ, Inserm, CNRS, Institut Paoli-Calmettes, CRCM, TrGET Platform, Marseille (France)

[5] Aix Marseille Univ, Inserm, CNRS, Institut Paoli-Calmettes, CRCM, Experimental Histo-Pathology Platform, Marseille (France)

[6] Knight Cancer Institute, Portland, OR 97201, USA

[7] Institut Universitaire de France (IUF)

[8] shared first authors

[9] shared senior authors

[10] corresponding authors: IBDM (Developmental Biology Institute of Marseille), 163 Avenue de Luminy, case 907, 13009 Marseille (France). F. Lamballe: fabienne.lamballe@univ-amu.fr; F. Maina: flavio.maina@univ-amu.fr

Competing interests: The authors declare no potential conflicts of interest.

Running title: Modeling TNBC heterogeneity shows WEE1 and BCL-XL necessity

Abstract

Triple-negative breast cancer (TNBC) is a highly aggressive breast cancer subtype characterized by a remarkable molecular heterogeneity and resistance to treatment. Here, we report the generation of a unique mouse model (*MMTV-R26^{Met}* mice) in which a subtle increase in the expression levels of the wild-type MET receptor tyrosine kinase leads to spontaneous, exclusive TNBC formation, recapitulating TNBC heterogeneity. We further exploited the *MMTV-R26^{Met}* TNBC model by exploring signaling alterations through proteomics to search for TNBC vulnerability. We identified a new drug combination based on combinatorial targeting of WEE1 and BCL-XL that efficiently kills TNBC cells. Mechanistically, we show that BCL-XL inhibition exacerbates the dependency of TNBC cells on WEE1 function, leading to Histone H3 and phosphoS_{33}RPA32 upregulation, RRM2 downregulation, cell cycle perturbation, and depletion of oncogenic signals, resulting in mitotic catastrophe and apoptosis. Our findings suggest that combination therapy with BCL-XL and WEE1 inhibitors warrants further evaluation in clinical trials.

Statement of significance

We have developed a new TNBC mouse model that recapitulates resistance to chemotherapy and heterogeneity. We uncovered that combined inhibition of WEE1 and BCL-XL selectively kills mouse and human TNBC cells, and provided mechanistic insights underlying this combined targeting. We propose that BCL-XL inhibition exacerbates WEE1 requirement for TNBC survival.

Introduction

Genetically engineered mouse models (GEMMs) of breast cancer have been proven as a powerful tool for gaining mechanistic insights into tumor initiation, progression, and metastasis as well as for developing innovative cancer therapy (1). GEMM models for breast cancer commonly use mammary-gland specific promoters, including MMTV (virus long terminal repeat), WAP (whey acidic protein), and C3 to ensure expression of transgenes in the mammary epithelium. More than 25 different murine GEMMs for breast cancer expressing different genes/oncogenes such as, *PyMT* (polyoma middle T antigen), SV40 T antigen, *ErbB2/Neu*, *cyclinD1*, *Ras*, *Myc*, *TGF-α*, and *Wnt1* have been established (2). The most widely used models are *MMTV-Neu* and *MMTV-PyMT*, which result in the development of multifocal adenocarcinoma and metastatic lesions in the lungs and/or lymph nodes. *MMTV-Neu* mice have been used for modelling epidermal growth factor receptor 2 (HER2)-positive breast cancer, whereas *MMTV-CyclinD1* for estrogen receptor (ER)-positive breast cancer. *MMTV-PyMT* mice lose the expression of ERα and progesterone receptor (PR) as they progress, but gain androgen receptor (AR) expression, therefore they have been used for modelling luminal AR positive TNBC (LAR) (3). However, only a small fraction of TNBC patients (~15%) are positive for AR, while the majority have been classified into different molecular subtypes, including basal-like (BL1 and BL2) and mesenchymal (M) (4,5).

TNBC, which accounts for approximately 10-15% of all breast cancer patients, is defined by the lack of ER and PR expression, as well as HER2 amplification/overexpression. Compared to the other breast cancer subtypes, TNBC is characterized by the earliest age of onset, a higher prevalence in African-Americans, a high propensity for metastasis, and the worst prognosis in terms of relapse and survival rate (6,7). Over 80% of TNBC patients exhibit alterations in the *TP53* locus (8), whereas a smaller fraction has mutations in genes controlling the PI3K pathway and homologous recombination including BRCA1/2 negative. A molecular feature of TNBC is the dependency of cancer cells on signals that are rarely mutated, a phenomenon defined as “non-oncogene addiction” (9). It is the case, for example, of components of the receptor tyrosine kinase (RTK) core pathway (7,10). Collectively, these traits are

among the leading cause of limited efficacy of current TNBC therapies. Radiation therapy and chemotherapy, applied before and after surgery, are the mainstay of treatment, although frequently associated with drug resistance and recurrent disease.

Extensive efforts have been made to search for molecular targeted therapies effective for TNBC treatment. Although some targeted therapies approved for treatment of other cancer types have been proposed in TNBC, they rarely turned out to be clinically relevant (11). These limited responses are associated with the high heterogeneity of the disease and the lack of suitable immunocompetent preclinical models that recapitulate the molecular diversity of TNBC. Among potential targets for TNBC subsets are PARP1, androgen receptor (AR), vascular endothelial growth factor receptor (VEGFR), epidermal growth factor receptor (EGFR), MET, PI3K/mTOR, MEK, Cyclin-dependent kinases (CDKs), heat shock protein 90 (HSP90), histone deacetylase (HDAC), hypoxia-inducible factor 1-α (HIF1-α), and integrins (7,11,12). Inhibition of WEE1 kinase has been proposed as a promising treatment option for TNBC and several other types of solid cancer (13,14). WEE1 plays central role in the G2/M checkpoint and controls DNA synthesis during the S phase as part of the S phase checkpoint. Therefore, inhibition of WEE1 is associated with accumulation of DNA damage and aberrant mitosis. Co-inhibition of WEE1 with either radiotherapy or anticancer drugs such as cisplatin, gemcitabin, paclitaxel, or inhibitors of CDC25, ATR, or PARP causes death of breast cancer cells (15-22). The rational of these combined treatments is to associate DNA-damaging therapies together with perturbation of DNA damage checkpoint gatekeepers through WEE1 targeting. Nevertheless, the consequences of WEE1 targeting may be broader than cell cycle regulation, in view of recent studies showing that WEE1 inactivation increases CDK-dependent firing of dormant replication origins thereby leading to replication stress and increased dNTP demand (23,24). Moreover, WEE1 was reported to modulate Histone H2B phosphorylation to inhibit transcription of several histone genes in yeast and humans (25) and to function as a histone-sensing checkpoint in budding yeast (25,26).

Here, we report the generation of a unique mouse model (*MMTV-R26*^{Met} mice) in which a subtle increase in the expression levels of the wild-type MET RTK leads to spontaneous TNBC formation. We

further exploited the *MMTV-R26*^{Met} TNBC model by exploring signaling alterations through proteomics and *MMTV-R26*^{Met} tumor properties both *in vivo* and *ex vivo*. A comprehensive integration of identified signaling alterations with datasets of TNBC patients through machine learning established that the *MMTV-R26*^{Met} model largely recapitulates TNBC heterogeneity. Furthermore, we identified a new drug combination based on a combinatorial targeting of WEE1 and of the anti-apoptotic factor BCL-XL that efficiently kills TNBC cells *in vivo*. Mechanistically, we show that BCL-XL inhibition exacerbates the dependency of TNBC cells on WEE1 functions, leading to epigenetic modifications such as Histone H3 upregulation and RRM2 downregulation, and to cell cycle perturbation, resulting in mitotic catastrophe and apoptosis. Our findings may be highly relevant for their potential translation to the clinic, also in view of promising studies of monotherapy with BCL-XL and WEE1 inhibitors in phase II clinical trials.

Results

Enhanced wild-type RTK MET expression levels in the mouse mammary gland induce spontaneous TNBC development

To specifically enhance wild-type MET levels in the mammary gland, we crossed the *MMTV-Cre* transgenic with *R26*^{stopMet} mice (referred to as *MMTV-R26*^{Met}). The specificity of the LacZ-stop cassette deletion obtained by the *MMTV-Cre* mice was evaluated using the *R26*$^{stopMet\text{-}Luc}$ mice (27), in which *Met*^{tg} is followed by an internal ribosome entry site-Luciferase reporter (Fig. 1A). *In vivo* imaging of female *MMTV-R26*$^{Met\text{-}Luc}$ mice revealed a strong luciferase signal in mammary glands only after the first lactation (Fig. 1B), consistent with the expression of the Cre recombinase following MMTV promoter activation by prolactin (28,29). This led to removal of the stop cassette, and thus *Met*^{tg} expression in the mammary gland of *MMTV-R26*^{Met} mice (Fig. 1A). Consistently, the Luciferase-positive domains further increased after the second lactation and were significantly reduced in post-lactating females, in agreement with involution of the mammary gland occurring when the lactation phase is over (Fig. 1B). This imaging analysis exemplifies the remodeling of the mammary gland overtime. In view of a dynamic regulation of the HGF/MET system in mammary gland morphogenesis previously reported (30,31), we assessed *Met* and *Hgf* mRNA levels in *MMTV-R26*^{Met} and control mice from the virgin to the post-lactation state. RT-qPCR analysis revealed comparable dynamics of *Met* and *Hgf* transcript expression in both *MMTV-R26*^{Met} and control mice: high levels at virgin state, a progressive downregulation during pregnancy, reaching almost undetectable levels during lactation, and a restoration of *Met* and *Hgf* levels at the post-lactation stage (Fig. 1C). Whereas *Met*^{tg} expression was undetectable in virgin animals, it became evident starting from the pregnancy stage, coherent with *MMTV* promoter activation by prolactin (28,29), and remained expressed during subsequent phases. Western blot analysis confirmed MET^{tg} expression in the mammary gland of *MMTV-R26*^{Met} mice (Fig. S1A).

We therefore hypothesized that the *MMTV-R26^{Met}* mice could be an appropriate genetic setting to assess the vulnerability of the mammary gland to subtle perturbation of wild-type MET levels overtime. In view of remarkable changes occurring during mammary gland morphogenesis, illustrated by our bioluminescence imaging and transcriptional analyses, and the susceptibility of parity-induced mammary epithelial subtypes to signaling perturbations (32), *MMTV-R26^{Met}* mice were kept under repeated cycles of pregnancy. Overtime, a proportion of *MMTV-R26^{Met}* mice spontaneously developed mammary gland tumors (Fig. 1D). Remarkably, the kinetic of tumor formation was similar to that of *MMTV-ErbB2* mice generated in the same genetic background we used as reference (*MMTV-ErbB2^{mix}*; Fig. 1D, S1B). The percentage of mice with tumors correlated with the severity in RTK alteration: 16% of *MMTV-R26^{Met}* mice (with enhanced wild-type MET) developed tumors (32/196) compared to 58% of *MMTV-ErbB2^{mix}* mice (with oncogenic HERBB2 overexpression; 11/19; Fig. 1D and S1B). A proportion of *MMTV-R26^{Met}* mice with mammary gland tumors also developed lung metastasis (19%; 6/32; Fig. S1C, Table S1). Histological analyses of the *MMTV-R26^{Met}* tumors revealed highly aggressive and infiltrating breast carcinomas, which have been histologically identified as being exclusively TNBC (24 tumors analyzed; Fig. 1E, Table S1). Proteomic studies were then performed through reverse phase protein array (RPPA), a high-throughput antibody-based technique to analyze protein activities in signaling networks. Analysis of expression and/or phosphorylation levels (247 signals, Table S2) displayed that the *MMTV-R26^{Met}* tumors (n=24) clearly segregate from control mammary glands (n=3; Fig. 1F). Interestingly, the *MMTV-R26^{Met}* tumors form 4 distinct clusters, highlighting heterogeneity in signaling levels, including MET phosphorylation status (Fig. 1F, G, S1D, Table S3). Heterogeneity was also observed at *Met* transcript levels, as revealed by RT-qPCR (Fig. S1E), reflecting the heterogeneity of *MET* levels among TNBC patients (33-35). Thus, a slight increase in *Met* levels in the mouse mammary glands is sufficient to trigger the tumorigenic program of TNBC.

Next, we explored the possibility to classify the *MMTV-R26^{Met}* tumors to TNBC subtypes by analyzing the RPPA data applying the Random Forest machine learning algorithm previously used with transcriptomic data (36). As subtype classification is usually done on transcriptomic data, we first used

the RPPA data of 152 TNBC patients from the TCGA dataset to build a model for subtyping prediction. We trained the model using 10-fold cross validation to optimize the method parameters (Fig. S1F). The model was sensitive to the M class (balanced accuracy 0.89), and had lower sensitivity in distinguishing between BL1 and BL2 classes (balanced accuracy of 0.69 and 0.55, respectively). This was done to take into account that most of the patients are BL1, with a consequent 30% correct BL1 prediction called "no information rate". Our Random Forest model had accuracy of 57% (or 71% without distinguishing BL1 and BL2), with a significance of p-value = 0.002 compared to the "no-information rate". We then applied the model on the RPPA data of *MMTV-R26^{Met}* tumors to predict their classification. Remarkably, we found that all TNBC subtypes are represented by the *MMTV-R26^{Met}* tumors with an enrichment of the mesenchymal subtype (Fig. 1H, I). Collectively, these results showed that a moderate increase of MET levels in the mammary gland is sufficient to perturb tissue homeostasis, is able to initiate the TNBC program including the formation of lung metastasis, and that the resulting tumors recapitulate the heterogeneity characteristic of TNBC patients.

The *MMTV-R26^{Met}* TNBC model recapitulates resistance to conventional chemotherapy and to a set of combined molecular treatments.

Six mammary gland tumor (MGT) cell lines were established from individual *MMTV-R26^{Met}* tumors and molecularly/biologically characterized (Fig. 2A). Four cell lines, MGT4, MGT9, MGT11, and MGT13 exhibited tumorigenic properties *in vivo*, illustrated by the formation of tumors when injected heterotopically into the flank of nude mice, whereas the two other lines, MGT2 and MGT7 did not (Fig. 2B). The four tumorigenic cell lines exhibited oncogenic features, whereas the MGT2 and MGT7 cell lines did not. In particular, we observed increased MET mRNA and protein levels (Fig. S2A-C), with a heterogeneity similar to that observed among *MMTV-R26^{Met}* tumors and reported in TNBC patients (34,35). MGT4, MGT11, and MGT13 (not MGT9) cell lines were capable of forming tumor spheroids when grown in self-renewal conditions (Fig. S2D, E). Additionally, the tumorigenic cell lines were characterized by a high proliferation index, with a low proportion of cells in the G0 cell cycle phase

(Fig. 2C, S3A-C). Cells of the tumorigenic lines also exhibited increased motility, particularly for MGT13 cells that display a rather mesenchymal-like morphology compared with the other cell lines (Fig. S2A, S3D). Biochemical studies revealed consistent upregulation of oncogenic signals in MGT4, MGT9, MGT11, and MGT13 compared with control cells. This included phosphorylation of MET, EGFR, of their downstream adaptor GAB1, of MEK/ERKs, AKT, RB and elevated anti-apoptotic signals such as MCL1, BCL-XL, and XIAP (Fig. 2D). Furthermore, these cell lines also recapitulated the heterogeneity of p53 alterations observed in TNBC patients: p53 overexpression (likely oncogenic) in MGT4 and MGT9, decreased expression of p53 in MGT13, and comparable p53 levels in MGT11 (Fig. 2E).

Next, we explored the sensitivity of tumorigenic MGT cells towards clinically relevant drugs and combined molecular treatments previously reported for TNBC. MGT4, MGT9, MGT11, and MGT13 cell lines were resistant to conventional chemotherapeutic agents, such as Docetaxel, Cisplatin, 5-Fluorouracil (5'FU), and only partially sensitive to Doxorubicin, although only at high doses (Fig. 2F). Furthermore, all these MGT cell lines were resistant to three drug combinations previously reported to be effective for TNBC treatment: combined inhibition of EGFR and MET (37), PI3K and MEK (38), and EGFR and PYK2 (39) (Fig. 2G). Together, these results show that the *MMTV-R26*^{Met}-derived cell lines are a relevant model to study drug resistance, an important feature of TNBC.

Combined targeting of WEE1 and BCL-XL is deleterious for TNBC cells

To further elucidate how *MMTV-R26*^{Met} MGT cells recapitulate molecular/signaling characteristics of TNBC, we examined their signaling status by RPPA and subsequent bioinformatics analysis (247 epitopes, listed in Table S2). The signaling profiles highlighted two major features, as illustrated by Principal Component Analysis (PCA). First, the tumorigenic MGT4, MGT9, MGT11, and MGT13 cells clearly segregate from the two types of non-tumorigenic cells: MGT7 and MGT2 (Fig. 3A, S4A, Table S4). Second, the four tumorigenic *MMTV-R26*^{Met} MGT cell lines fall into two distinct TNBC subtypes that we named "subtype A" for MGT4, MGT9, MGT11, and "subtype B" for MGT13 (Fig. 3A, S4A, Table S4). To obtain insights on molecular and cellular functions characterizing "subtype A" from "subtype

B", we performed a series of enrichment analyses by applying Enrichr, a web-based tool to highlight enrichments based on gene sets. Both subtypes showed an enrichment in pathways related to DNA repair, cell cycle regulation, and metabolism (Fig. 3B, S4B). These enrichments are consistent with enhanced proliferation capacity of MGT4, MGT9, MGT11, and MGT13 cells versus non-tumorigenic cells. Moreover, "subtype B" is enriched in pathways related to stemness properties (Fig. 3B, S4B), consistent with the enhanced capability of MGT13 to form tumor spheroids *in vitro.*

Inspired by these signaling profiles, we designed a drug screen aiming at identifying combinatorial treatments effective for the two subtypes of TNBC cells modelled by the MGT lines (see Methods). Among all treatments (single or combined drugs) tested in the MGT4 cell line, we uncovered that the simultaneous inhibition of BCL-XL and WEE1 drastically reduced tumor cell viability (Fig. 3C, D). By further assessing the effects of this combined treatment on the six *MMTV-R26^{Met}* MGT cell lines, we found that BCL-XL+WEE1 inhibition was deleterious for all four tumorigenic *MMTV-R26^{Met}* MGT cells (MGT4, MGT9, MGT11, MGT13), but not for the non-tumorigenic cells (MGT2 and MGT7; Fig. 4A, B). Importantly, this highlights lack of a nonspecific *in vitro* toxic effect of the newly identified drug combination. Combined inhibition of BCL-XL and WEE1 was synergistic (for 3 out of 4 *MMTV-R26^{Met}* MGT cell lines), as shown by the Bliss score and by the Chou-Talalay combination index score calculation (Fig. 4A, S5A). Furthermore, BCL-XL+WEE1 targeting was detrimental for all six human TNBC cells tested (Fig. 4C). Intriguingly, when this drug combination was tested on human non-TNBC cells, we found that inhibition of BCL-XL did not exacerbate the effects elicited by WEE1 targeting (Fig. 4D), indicating that WEE1 inhibition is particularly detrimental in TNBC cells. Recent studies have reported the sensitivity of TNBC to WEE1 targeting in the presence of either PARP or ATR inhibitors, or Cisplatin (17,19,20,22,40). However, we found that *MMTV-R26^{Met}* MGT cells were either resistant or only partially sensitive to these drug combinations (Fig. 4E), recapitulating other mechanisms of resistance beside those reported in Fig. 2F and G. Thus, inhibition of BCL-XL exacerbates the requirement of WEE1 in this TNBC model. Finally, to assess *in vivo* the effect of combined BCL-XL+WEE1 targeting on tumor growth, we engineered a cell line for *in vivo* imaging by stably transfecting the MGT11 cell line,

characterized by strong tumorigenic properties, with a Luciferase reporter vector (defined as $MGT11^{Luc}$). We confirmed the $MGT11^{Luc}$ cells to have comparable biological properties as the parental cells, and to maintain sensitivity to combined BCL-XL+WEE1 targeting (Fig. S5B-D). Orthotopic studies showed that combinatorial BCL-XL+WEE1 inhibition reduced *in vivo* tumor growth of $MGT11^{Luc}$ cells injected into the mammary fat pad of mice (Fig. 4F-I, S5E). No obvious effects on mouse viability or murine weight indicated the lack of toxicity. Thus, the *MMTV-R26^{Met}* model recapitulating heterogeneity and resistance of TNBC led us to uncover a new potent drug combination based on BCL-XL and WEE1 inhibition, effective on human TNBC cell lines characterized by distinct features.

BCL-XL inhibition exacerbates WEE1 requirement in TNBC cells

While BCL-XL primarily has an anti-apoptotic function by inhibiting cytochrome C release, WEE1 acts on multiple regulatory circuits. Besides its well-established involvement in regulating the G2/M transition through phosphorylation of CDK1, recent studies have highlighted additional mechanistic roles of WEE1 in DNA replication stress and regulation of histone synthesis and levels. Therefore, we thoroughly examined the signaling changes occurring following BCL-XL and WEE1 inhibition in MGT cell lines by RPPA analysis (426 epitopes were analyzed, Table S2); some changes were validated by Western blot analyses. As examples, the profile of proteins differentially expressed and/or phosphorylated in MGT4 and MGT11 is displayed in Fig. 5A and B, respectively. Interestingly, while BCL-XL inhibition alone had modest effects, WEE1 inhibition had marked effects on the cells, many of which were accentuated by treatment with the BCL-XL inhibitor. Among identified changes, some were consistently observed in all MGT cell lines, whereas others were specific to individual MGT lines (Fig. 5C, D, Table S5). These changes covered a broad range of signaling/cellular functions, such as those associated with cell survival/death, cell cycle regulation, DNA damage/repair, histone levels, and oncogenic properties (Fig. 5A, B).

Consistent with the well-known regulatory activity of WEE1 in cell cycle progression, we observed decreased levels of phosphoY_{15}CDK1 (the direct target of WEE1), phosphoS_{795}RB, and CHK1 expression

upon WEE1 inhibition (Fig. 5D, 6A, Table S5). This was accompanied by an alteration in the distribution of cells in cycle phases as shown by FACS profiles (Fig. 6B). Concerning cell survival signals, combined BCL-XL+WEE1 targeting in MGT cells led to a drastic down-regulation of MCL1 and XIAP anti-apoptotic signals associated with intense cleavage of Caspase3 and PARP (Fig. 5A, 5B 6A). Regarding DNA damage and repair, we observed an up-regulation of phosphoS_{1987}ATM and phosphoS_{139}H2AX (histone variant, γH2AX) reflecting increased levels of DNA damage in the MGT cell lines upon treatment (Fig. 6A, S6A). This high proportion of DNA damage is associated to the downregulation of Rad51 (Fig. 5A, 5B, 5D), which plays a major role in DSB repair by homologous recombination and in fork protection, and restart during replication stress (41), raising the possibility that this down-regulation is related to the increase of phosphoS_{139}H2AX. Moreover, we observed a drastic downregulation of RRM2, a subunit of the ribonucleotide reductase required to maintain high levels of dNTPs as previously reported (23), with an upregulation of Histone-H3 and H3K9me2 levels (Fig. 5, 6C-E, S6B, Table S5). This was further confirmed by cell fractionation studies, showing downregulation of RRM2, and increase of pS_{33}RPA32 in the chromatin fraction of cells co-treated with WEE1 and BCL-XL inhibitors (Fig. 6E). Finally, concerning oncogenic signals, we found a significant downregulation of phosphorylation levels of MET and GAB1 (Fig. 6A). Collectively, these results indicated that BCL-XL inhibition exacerbates the dependence of TNBC cells on the overall functions exerted by WEE1: an intact dNTP pool (by stabilizing RRM2 protein levels), appropriate histone levels, and proper cell cycle progression through G2/M.

Combined BCL-XL and WEE1 inhibition leads to mitotic catastrophe and apoptosis of TNBC cells

We explored at cellular levels the biological events associated with BCL-XL and WEE1 inhibition by immuno-cytochemistry. In cells experiencing the combined treatment, we found a significant increase in the number of γH2AX-positive cells as well as a raise in intensity of γH2AX staining per cell reflecting an accumulation of DNA DSBs (Fig. 7A). These findings are in agreement with the above results (Fig. 6A) and reflect increased DNA damage in a high proportion of cells following BCL-XL+WEE1 targeting. In addition, we found a striking increase in phosphoS_{10}Histone H3 (pH3)-positive cells when subjected

to the combined treatment (Fig. 7B), suggesting that a high proportion of cells are in G2/M (42). This could reflect a premature entry in mitosis due to WEE1 inhibition, but also an accumulation of unrepaired DNA damage in mitosis (13,43). We investigated the consequences of this premature mitotic entry by performing a double immuno-staining with anti-α-Tubulin and anti-pH3 antibodies in cells treated (or not) with BCL-XL+WEE1 inhibitors. Interestingly, the staining highlighted a marked increase of cells harboring mitotic catastrophes revealed by monopolar, multipolar or disorganized spindles, and even cytokinesis failure (Fig. 7C). The results further showed that BCL-XL inhibition exacerbated the effects of WEE1 targeting by forcing the cells to exit mitosis without undergoing complete chromosome segregation, a phenomenon called mitotic slippage. As a consequence, these excessive unscheduled and abnormal mitosis events led to an increased formation of micronuclei in treated cells (Fig. 7D).

Finally, we assessed the terminal event associated with combined BCL-XL and WEE1 targeting on TNBC cells. We found that a pan-Caspase inhibitor (Z-VAD-FMK) significantly rescued cell death caused by the combined treatment of TNBC cells (Fig. 7E, F). This result was consistent with Western blots analysis showing a strong increase in Caspase3 and PARP cleavage upon combined BCL-XL+WEE1 inhibition (Fig. 6A). In contrast, inhibition of ferroptosis, another cell death mechanism to which TNBC cells are highly sensitive (44), did not prevent cell death (Fig. 7E, F). Together, these findings indicate that the combined targeting of BCL-XL and WEE1 exacerbates the dependency of TNBC cells on WEE1 function in a context of low anti-apoptotic inputs, leading to mitotic catastrophe and apoptosis.

Discussion

In this study, we have developed a new TNBC mouse model that recapitulates resistance to chemotherapy, we uncover that the combined inhibition of WEE1 and BCL-XL selectively kills mouse and human TNBC cell lines, and provide mechanistic insights into inhibition of WEE1 and BCL-XL in TNBC cells. We propose that WEE1 is an attractive target for TNBC therapies.

A number of transgenic mice have been engineered to model TNBC, predominantly through drastic genetic manipulations (often combined), such as loss-of-tumor suppressors and overexpression of activated oncogenes (45). Although they have been instrumental to implicate candidate genes as oncogenes, each model generally recapitulates a fraction of disease features predominantly associated with the genetic manipulation employed. Patient-derived xenografts (PDXs) capture the heterogeneity that characterizes cancers like TNBC. However, transplantation-based models in immunocompromised mice do not report on the reciprocal crosstalk between cancer and immune cells, a limitation that can be overcome, in part, by laborious and expensive "humanized models". However, most murine TNBC models do not recapitulate the formation of spontaneous cancers occurring in human patients. In this respect, the *MMTV-R26*^{Met} model is rather unique for a series of features.

(i) Tumors developed by *MMTV-R26*^{Met} mice are exclusively TNBC rather than covering a range of breast cancer types. This is not the case for other transgenic mice overexpressing MET oncogenic forms in the mammary gland (46-49), generated in the past because of implication of MET in breast cancer pathophysiology. Indeed, MET is overexpressed in about 40% of breast cancer patients (in luminal A: 36%; in Luminal B: 39%; in HER2+: 48%; in TNBC: 53% (50)), and its overexpression often correlates with poorly differentiated and aggressive forms of the disease (34). In TNBC, MET is particularly highly expressed, and implicated in malignancy progression, metastasis, and resistance to anticancer therapies (33,34). Consequently, agents targeting MET are actively being explored for clinical purposes (51,52), including in TNBC (53-55).

(ii) In *MMTV-R26^{Met}* mice, the TNBC program is driven by a subtle increase of MET levels in the mammary gland (about 3-folds), and by the wild-type form of MET rather than oncogenic versions of MET (mutated MET or TPR-MET) (46-48). Consequently, *MMTV-R26^{Met}* TNBC cells are not addicted to MET, a feature predominantly characterizing cancers induced by driver oncogenes. This might explain why the *MMTV-R26^{Met}* model reported here recapitulates the tumor heterogeneity typical of TNBC patients.

(iii) TNBC heterogeneity is recapitulated by *MMTV-R26^{Met}* mice at different levels.

(iv) *MMTV-R26^{Met}* TNBC recapitulates resistance to conventional chemotherapy and to a set of targeted molecular treatments reported in previous studies (38).

Histologically, the 28 *MMTV-R26^{Met}* tumors analyzed revealed differences in their grade (although the majority were high-grade), with a range of low to high mitotic index, and the absence or presence of necrotic areas. Heterogeneity is also evidenced by processing our RPPA analysis of 24 *MMTV-R26^{Met}* tumors through machine learning, indicating that the 4 TNBC subtypes (BL1, BL2, LAR, and mesenchymal) are indeed represented, with the most aggressive mesenchymal subclass enriched. Diversity was preserved *in vitro* by the four *MMTV-R26^{Met}* MGT cells we established from distinct tumors. Heterogeneity is maintained even concerning MET levels in TNBC, as shown for example by the different levels of MET expression and activation in *MMTV-R26^{Met}* tumors and cells (for example, phosphorylation levels of MET and of GAB-1, a MET downstream effector). It is tempting to speculate that although all tumors in *MMTV-R26^{Met}* mice originate from a common genetic setting characterized by a slight increase of MET levels, this context does not impose an oncogenic path in which MET would be systematically altered in all tumors to the same extent. Finally, *MMTV-R26^{Met}* MGT cells are also heterogeneous in terms of drug sensitivity: for example, while MGT9 and MGT11 are resistant to single WEE1 targeting, MGT4 and MGT13 are partially sensitive.

It is rather surprising that a subtle increase of MET levels, in its wild-type form, spontaneously initiates a destabilization process that fully recapitulates the whole TNBC program. Nevertheless, this sensitivity

to MET levels is conditioned by a multiparous context, as females without multiple pregnancies did not develop tumors. Both MET and HGF are dynamically expressed during pregnancy/lactation, as we showed here consistent with previous reports (30,31). Moreover, the HGF/MET system regulates mammary gland morphogenesis, especially ductal branching and proliferation of ductal end buds (56). These data illustrate how a tight regulation of the time and signal input levels required for the mammary gland remodeling is critical to prevent transformation. The vulnerability of the mammary gland to a slight increase in MET levels resembles the susceptibility of the liver we reported in previous studies (27,57-59). The vulnerability of the mammary gland and the liver is contrasted by a remarkable resilience of other tissues, in which a tumorigenic event requires additional genetic alterations, as reported for malignant peripheral nerve sheath tumors (60). Whether such a mild MET perturbation in the mammary gland occurs in specific subgroups of women and/or physiological contexts and can increase susceptibility to tumor development remains an open issue. If this is not the case, such genetic manipulation nevertheless makes it possible to initiate a cascade of molecular events leading to a clinically relevant TNBC context. We therefore propose the *MMTV-R26*^{Met} genetic setting as a relevant model, complementary to others, for molecular and preclinical studies on TNBC in an immunocompetent context. Moreover, the panel of *MMTV-R26*^{Met} MGT cells we generated may be particularly useful to screen therapeutic options targeting TNBC resistance.

The second major finding of this work is that combinatorial inhibition of WEE1 and BCL-XL kills a panel of heterogeneous *MMTV-R26*^{Met} and human TNBC cell lines. For decades, WEE1 has been considered primarily as a key regulator in cell cycle progression (13,14). In particular, WEE1 regulates the G2/M checkpoint through phosphorylation and inactivation of CDK1, thus preventing entry of cells with unrepaired DNA damage into mitosis (13). Nevertheless, additional mechanistic functions of WEE1 have recently emerged. Indeed, WEE1 stabilizes RRM2 protein, a regulatory subunit of the ribonucleotide reductase required to maintain high dNTPs levels (23). In addition, WEE1 was reported in yeast and human to inhibit transcription of several histone genes by phosphorylating Histone H2B at Tyr_{37} (25). In addition, the WEE1 yeast homolog $Swe1^{WEE1}$ was recently reported to act as a histone-

sensing checkpoint by sensing excess histone levels before cells enter mitosis, thus preventing aberrant chromosomal segregation and polyploidy (26). Thus, WEE1 targeting might affect several key cellular processes that are particularly relevant in cancer cells as they proliferate at high rates and are more prone to replication stress with higher demands in dNTP and histones. WEE1 inhibition may therefore particularly expose cancer cells to DNA damage. This is reflected by the marked increase of cells harboring mitotic catastrophes upon the combined inhibition of WEE1 and BCL-XL in TNBC cells.

WEE1 is an attractive target for cancer therapies including for TNBC, and strategies are being intensively explored in preclinical studies and clinical trials. It has been recently reported that WEE1 targeting, in combination with either cisplatin or inhibitors of ATR or PARP is effective in human TNBC cells lines (17,19,20,22,40). By testing them in *MMTV-R26*^{Met} MGT cells, mimicking resistant treatment contexts, we have shown that these three combinations are indeed effective, albeit to a varying degree and depending on the cell line. Nevertheless, the combinatorial targeting of WEE1 together with BCL-XL elicits superior effects, as shown by the loss of viability of all four very aggressive/highly tumorigenic *MMTV-R26*^{Met} MGT cell lines and of the six human TNBC cell lines tested. Interestingly, such vulnerability is specific to TNBC cells as three out of four non-TNBC cell lines were resilient to WEE1 plus BCL-XL inhibition. This resilience, as well as the absence of effects on two non-tumorigenic *MMTV-R26*^{Met} MGT cell lines (MGT2, MGT7) highlights two relevant points. First, the reduction of the stress support pathway by targeting BCL-XL exacerbates a specific requirement of WEE1 in TNBC. This effect resembles an “essentiality-induced” synthetic lethality, characterized by the essentiality of one gene following the targeting on a second gene (61). Nevertheless, we cannot exclude that BCL-XL targeting may also contribute to altered cell cycle progression (62). Second, in addition to the absence of *in vivo* side effects, BCL-XL plus WEE1 targeting appears to be a rather safe treatment for healthy cells. Thus, our findings may be particularly relevant from a translational perspective, considering that agents targeting WEE1 or BCL-XL are already in phase I/II clinical trials.

Methods

Mice

Ethics statement: All procedures involving the use of animals were carried out in accordance with the European Community Council Directive of 22 September 2010 on the protection of animals used for experimental purposes (2010/63/EU). The experimental protocols were performed according to the institutional Ethical Committee guidelines for animal research (Comité d'éthique pour l'expérimentation animale – Comité d'éthique de Marseille) and in compliance with the French law under the agreement number D13-055-21, delivered by the "Préfecture de la Région Provence-Alpes-Côte-d'Azur et des Bouches-du-Rhône". Mice were housed under pathogen-free conditions in enriched cages, with a light/dark cycle, and fed ad libitum according to Safe Complete Care Competence (SAFE A04). The mouse project authorization of the Maina laboratory is: APAFIS #8214-2016121417291352.v5, delivered by the "Ministère de l'Enseignement Supérieur, de la Recherche et de l'Innovation".

R26^{stopMet} mice (international nomenclature *Gt(ROSA)26Sor*$^{tm1(Actb\text{-}Met)Fmai}$), and *R26*$^{stopMet\text{-}Luc}$ mice (international nomenclature *Gt(ROSA)26Sor*$^{tm1(Actb\text{-}Met\text{-}IRES\text{-}Luc)Fmai}$) carrying a conditional mouse-human chimeric *Met* transgene in the *Rosa26* locus was previously reported (63,64). In both lines, expression of the MET^{tg} (with or without Luciferase) was conditioned by the Cre-mediated removal of a LoxP-stop-LoxP cassette. *MMTV-R26*^{Met} and *MMTV-R26*$^{Met\text{-}Luc}$ transgenic mouse lines were generated by crossing the *R26*^{stopMet} or *R26*$^{stopMet\text{-}Luc}$ mice, respectively, with the *MMTV-Cre* line (B6129-Tgn(MMTV-Cre)4Mam) obtained from the Jackson Laboratory. All animals were maintained in a mixed genetic background (50% 129/Sv, 50% C57/Bl6). Mice were genotyped by PCR analysis of genomic DNA as described elsewhere (63,64). Since it has been well established that mammary gland tumor formation is accelerated in multiparous females (32), *MMTV-R26*^{Met} mice were maintained in constant breeding. Eight week-old nude mice (Rj:NMRI-Foxn1 nu/nu; JanvierLabs) were used for xenograft studies. Healthy 8-week-old female NOD.Cg-Prkdc ^{scid}/J (NSG) mice, used for orthotopic studies, were bred in

the animal facility of the Cancer Research Center of Marseille (CRCM) and maintained under specific pathogen-free conditions with sterilized food, water provided ad libitum and on a 12-h light and 12-h dark cycle. Orthotopic experiments were approved by animal ethics committees (APAFIS#13349-2018013116278149 v2).

In vivo bioluminescence imaging

Imaging was conducted as previously described (27). Briefly, anesthetized *MMTV-R26*$^{Met\text{-}Luc}$ mice were injected intraperitonealy with luciferin (3 mg/mouse). Analysis of the luminescent images was performed using Berthold Technologies software.

Immunohistochemistry

For histopathological analysis, control mammary glands or dissected tumors were fixed for 4hrs in 4% paraformaldehyde (PFA, Sigma), processed for paraffin embedding, and sectioned. They were then either stained with hematoxylin, and counterstained with eosin (H&E) or subjected to immunostaining with antibodies directed against estrogen receptor (ER), progesterone receptor (PR), human EGFR2 (HER2), or Ki67 (antibodies, and dilutions used are listed in Table S6).

Cell lines

MMTV-R26^{Met} MGT cell lines were derived from independent *MMTV-R26*^{Met} tumors. To establish *MMTV-R26*^{Met} MGT cell lines, *MMTV-R26*^{Met} tumors were dissected, and chopped into 1 mm3 pieces. Cells were dissociated for 30-40 min at 37°C with type II collagenase (1mg/ml, ThermoFisher Scientific) and DNase I (20µg/ml, Roche) in DMEM/F12 (Dulbecco's modified Eagle's media/F12, 1/1, ThermoFisher Scientific) complemented 10% fetal bovine serum (FBS, ThermoFisher Scientific), penicillin-streptomycin (P/S, 100 U/ml/0.1 mg/ml, ThermoFisher Scientific), and fungizone (25µg/ml, Sigma). The cell suspension was then passed through a 40µm nylon cell strainer to remove aggregates, and cells were seeded in complete DMEM/F12 medium (DMEM/F12, supplemented with 10% FBS, P/S,

glutamine (2mM, ThermoFisher Scientific), glucose (0.25%, Sigma), insulin (10 µg/ml, Sigma), transferrin (10µg/ml, Sigma), sodium selenite (5ng/ml, Sigma), hydrocortisone (0.5 µg/ml, Sigma), EGF (20ng/ml, Roche), and HGF (10 ng/ml, Peprotech), and cultured in this complete medium in a humidified incubator at 37C° in a 5% CO_2 atmosphere. The establishment of normal mammary epithelial cell culture was performed as described above. Mammary glands were dissected from *MMTV-R26*^{Met} mice not carrying tumor.

Human TNBC (MDA-MB-231, MDA-MB-468, SUM-159, Hs578t, HCC-1937 and BT-549) and non-TNBC (MCF-7, SKBR-3, and BT-474) cell lines were obtained from the American Type Culture Collection (ATCC). All human breast cancer cells were grown in DMEM/F12 medium supplemented with P/S, glutamine (2mM), sodium pyruvate (1mM, ThermoFisher Scientific), non-essential amino acids (ThermoFisher Scientific), and insulin (10µg/ml; Sigma).

MGT11^{Luc} cells were generated by lentivirus infection of the parental *MMTV-R26*^{Met} MGT11 cells. Briefly, the pHAGE PGK-GFP-IRES-LUC-W lentivirus construct, which allows expression of luciferase and GFP in the infected cells, was used to produce the lentivirus and perform infection. Infected cells were grown in complete DMEM/F12 medium. GFP-positive cells were then sorted by FACS, amplified, and tested for their bioluminescence. All cells were tested by PCR-based assay to assess their mycoplasma-free status.

Drugs

Drug concentration and sources are reported in Table S7. Calculation of the Synergy maps and Bliss score has been done using online SynergyFinder tool v1.0 (65) using "Viability" parameter as readout and "Bliss Method" with correction activated.

Synergy or additive effects of drug combinations were measured by employing the CompuSyn software v1.0 using the Chou-Talalay equation. Combination index CI<1 indicates synergism, CI<0.5 indicates strong synergism, CI=1 means additive effect and CI>1 stands for antagonism.

Cell viability assay

MMTV-R26^{Met} MGT and human breast cancer cells were plated in 96-well plates at 10,000 cells per well (150µl media/well). After 24hrs, cells were treated with single or combined drugs at the indicated concentrations (Table S7) and cell viability was assessed 48hrs later using the Cell Titer Glo Luminescent Assay (Promega) by detecting the luminescent signals with a luminometer microplate reader (Berthold). Concerning cell death rescue experiments, *MMTV-R26^{Met}* MGT and MDA-MB-231 cells were pre-treated for 1hr with inhibitors of apoptosis (Z-VAD-FMK) or ferroptosis (Ferrostatin-1) at the indicated concentrations, then for additional 24hrs in the absence or presence of A-1155463 (0.3µM) and Adavosertib (3µM). Effects of cell death inhibitors on specific death inducers were assessed as positive control. Data are mean values of at least three independent experiments done in triplicates.

Cell cycle analysis by flow cytometry

MMTV-R26^{Met} MGT cells were cultured in standard conditions before cell cycle analysis of non-treated cells. Regarding cell cycle analysis after drug treatment, cells were treated with vehicle, A1155463 (1µM), Adavosertib (3µM), alone or in combination for 12hrs. After trypsinisation, cells were resuspended at 10^6 cells per condition. Single cell suspensions were first incubated with the antibodies indicated in Table S6 and Fixable Viability Dye eF506 (1:1000, eBioscience) in PBS-0.5% BSA for 20 min at 4°C. Cells were then fixed and permeabilized using eBioscience™ Foxp3 / Transcription Factor Staining Buffer Set, according to manufacturer's instructions. After centrifugation, cells were resuspended in permeabilization solution containing anti-Ki67antibody, propidium iodide (PI, 40µg/ml, ThermoFisher Scientific) supplemented with RNaseA (50µg/ml, ThermoFisher Scientific). Cells were incubated 20 minutes at room temperature, washed and rapidly analyzed by a BD LSR-II FACS (lasers 405, 488, 561, and 633nm). Cell cycle distribution was analyzed with the BD-Diva version 8.0.1 software. Three independent experiments were performed.

Apoptosis assay by flow cytometry

Quantification of apoptosis was assessed by Annexin V-PI staining, using the eBioscience™ Annexin V Apoptosis Detection Kit FITC, according to the manufacturer's instructions. Briefly, harvested cells were washed in cold PBS and incubated for 15 minutes at room temperature with Annexin V-FITC / PI (1µg/ml) solution prepared in binding buffer. Samples were rapidly analyzed by a BD LSR-II FACS (lasers 405, 488, 561, and 633nm). Results were analyzed with BD-Diva version 8.0.1 software. Four independent experiments were performed.

Cell migration assay

MGT cells (10^4) were seeded in the upper compartment of an 8µm-pore Boyden-like chamber (Transwell, Corning) in 200µl of DMEM/F12 complete medium supplemented with 0.5%FBS. To create a chemo-attractant gradient, the bottom chambers were filled with 700µl of complete DMEM/F12 medium containing 10%FBS, 20ng/ml EGF, 10ng/ml HGF. Media also contained Cytosine arabinoside (AraC, 10µM) to prevent cell proliferation. After 36hrs of incubation at 37°C, non-migrating cells present on the upper surface of the filter were removed with a cotton swab. The invading cells located on the underside were fixed with 4% PFA, and nuclei were stained with DAPI. The number of migrating cells was directly analyzed under a Zeiss Axiophot fluorescent microscope, and determined in at least five fields of each filter. Experiments were performed in triplicate in three independent experiments.

Tumor spheroid forming assay

Cells were seeded in 35mm low attachment plates at a density of 25,000 cells/dish in DMEM/F12(1:1) medium supplemented with P/S (50mg/ml), glutamine (2mM), bovine serum albumin (BSA, 0.01%, Sigma), B27 without vitamin A (2%, ThermoFisher Scientific), N2 supplement (1%, ThermoFisher Scientific), insulin (10µg/ml), hydrocortisone (0.5 µg/ml), EGF (20ng/ml), HGF (10 ng/ml), and bFGF (10ng/ml, ThermoFisher Scientific). Medium was changed every 2 days. After 10 days, primary spheres were dissociated into single cells and re-plated at the same density as previously described.

Subspheroid forming assay (also called passage) was repeated every 10 days. Brightfield pictures of the whole dishes were acquired using an inverted Zeiss Axiophot microscope. Number and size of tumor spheroids were determined using the ImageJ software. Values are expressed as mean ± SEM of three independent experiments.

β-Gal and immunofluorescence staining on MGT cells

For β-Gal staining, cells cultured on glass coverslips were fixed for 2 min in PBS, 25% Gluteraldehyde, 37% formaldehyde, then washed with PBS, and incubated with the staining solution (1mg/ml X-Gal, 0.5mM K3K4, 2mM MgCl2 in PBS) for 4hrs at 37°C. Cells were then fixed with 4% PFA, counterstained with eosin, and mounted on glass microscopic slides with Eukitt hardening solution.

For immunofluorescence staining, cells cultured on coverslips and fixed with 4% PFA were permeabilized for 15 min in PBS/TritonX-100 (PBST) solution (see TritonX-100 concentrations in Table S6), incubated for 1hr in blocking solution (PBST, 10% BSA), then overnight at 4°C with primary antibodies (MET, $pY_{1234/1235}$MET, Ki67) diluted in the above blocking solution. The next day, cells were washed 4 times with PBST, subsequently incubated for 1hr with fluorescence-labelled secondary antibodies (Table S6), incubated for 15 min in presence of DAPI (1:1000), then mounted on glass microscopic slides with Prolong Gold antifade reagent (ThermoFischer Scientific). Images were taken with a Zeiss Axiophot fluorescent microscope.

***In vivo* tumorigenesis assays**

<u>Xenografts.</u> To assess the *in vivo* tumorigenicity of the *MMTV-R26^{Met}* MGT cell lines, cells ($5x10^6$) were resuspended in 200µl of a PBS:Matrigel (1:1) solution (CorningBV), and injected subcutaneously into both flanks of nude mice (n=4 mice / cell line). Animals were sacrificed when the tumor volume reached a maximum of 2000 mm^3. Tumor volume, measured with a caliper, was determined by the formula: $(L \times W^2)/2$. L: length; W: width.

Orthotopic injections. To evaluate the *in vivo* efficacy of the drug combination, MGT11^{Luc} (1x10^5) cells, suspended in 50% phenol red–free Matrigel (Becton Dickinson Bioscience), were grafted into the fourth mammary fat pad of NSG mice (TrGET Preclinical Platform). After seven days of graft, mice were randomly divided into two groups (n=8 per group). Starting from the eighth day post-graft, control vehicle (2% DMSO, 30% PEG300, 5% Tween-80) or drug combination were administered (A1155463, 5mg/Kg, intraperitoneally; Adavosertib, 60mg/Kg, *per os*) for a total of 29 days. Mice body weight was checked daily, before drug administration. Tumor volume was measured every three days and calculated with the formula: (3.14 x Length x Width x Height)/6. The experiment was terminated when tumor volume reached a maximum of 1500mm^3. After completion of the study, lung luminescence was assessed following addition of endotoxin-free luciferin (30 mg/kg) and autopsy of mice. Bioluminescence analysis was performed using Optima-PhotonIMAGER (Biospace Lab).

Quantitative RT-PCR analysis

Total RNA was extracted from tissues or cells using the RNeasy Mini Kit (Qiagen) as previously described (57). DNase (RNase-free DNAse I Set, Qiagen) treatment was included to avoid possible genomic DNA contamination. cDNA was synthesized using a Reverse Transcription Kit (iScript Reverse Transcription Supermix, Bio-Rad). Real-time PCR reactions were performed in a qPCR CFX 96 apparatus (Bio-Rad), using the SYBR® Green detection method (SYBR GreenER qPCR SuperMix, ThermoFisher Scientific), and specific primers (0.1µM; primer sequences are listed in Table S8). mRNA expression levels were normalized to the *Beta-2-microglobuline* (*B2M*) housekeeping gene, and analyzed using the $2^{-\Delta\Delta Ct}$ method. All reactions were run in triplicate and repeated in three independent experiments.

Western blotting

Protein extracts were biochemically analyzed as previously described (66). Briefly, *MMTV-R26^{Met}* MGT cells were lysed in EMB lysis buffer (1% Triton X-100, 50mM HEPES, 1mM EGTA, 150mM NaCl, 1.5mM MgCl2, 10% glycerol, 10mM NaF, 1mM NaPP, 1mM Na_3VO_4, 10mM β-glycerophosphate, 5µg/ml

leupeptin, 5 µM pepstatin A, 2µg/ml aprotinin, 5mM benzamidin, 1mM phenylmethylsulfonyl fluoride (PMSF), and centrifuged at 14,000 rpm for 15 min at 4 °C. Protein concentration was measured by Bradford assay (Bio-Rad), and equal amounts of proteins were separated on 10% polyacrylamide gels or SDS-PAGE (for phospho-ATM).

For nuclear and chromatin extracts, cells were pelleted, washed in PBS, swollen in hypotonic buffer (20mM HEPES pH 7.9, 1.5mM MgCl2, 10mM KCl, 1mM DTT, 1mM PMSF, 1x protease Inhibitor cocktail (Sigma)) on ice, then centrifuged at 1500rpm for 5min. Nuclei were resuspended in nuclear extract low salt buffer (20mM HEPES pH 7.9, 350mM sucrose, 1.5mM MgCl2, 150mM KCl, 0.5mM EDTA, 0.2% NP-40, 1mM PMSF, 1x protease Inhibitor cocktail) for 30 min on ice. The nucleoplasmic extract was recovered in the supernatant after centrifugation at 3000rpm for 10min. Residual nuclei were then resuspended in nuclear extract buffer (20mM HEPES pH 7.9, 350mM sucrose, 1.5mM MgCl2, 300mM KCl, 0.5mM EDTA, 0.2% NP-40, 1mM PMSF, 1x protease Inhibitor cocktail). After centrifugation at 3000rpm for 10min, the nuclear extract (supernatant) was separated from the chromatin (pellet). DNA from pellet was digested with Universal Nuclease (PierceTM) in nuclear extract high salt buffer (20mM HEPES pH 7.9, 350mM sucrose, 1.5mM MgCl2, 600mM KCl, 0.5mM EDTA, 0.2% NP-40, 1mM PMSF, 1x protease Inhibitor cocktail) for 30 min on ice. Protein concentration was measured by Qubit Protein Assay Kit (ThermoFisher) and equal amounts of proteins were separated on 15% polyacrylamide gels.

Membranes were incubated in blocking buffer (5% milk, PBS, 0.1% Tween-20, 50mM NaF), then analyzed using standard procedures. PageRuler Plus Prestained protein ladder (ThermoFisher Scientific) was used as a molecular weight marker. Pictures of the membranes stained with Ponceau (Sigma) and immunoblotted were taken through BioRad ChemiDoc imager. Antibodies used are reported in Table S6.

Reverse phase protein array (RPPA)

Protein lysates of dissected mammary gland tumors (n=24), control mammary glands (MMTV and *MMTV-R26^{Met}*), and *MMTV-R26^{Met}* MGT cells either not treated or treated for 12hrs with A1155463

(1µM), Adavosertib (3µM), or A1155463 + Adavosertib (1µM, 3µM) were prepared according to the MD Anderson Cancer Center platform instructions. Samples were screened with 426 antibodies to identify signaling changes in protein expression and phosphorylation levels.

Bioinformatic analysis

Random Forest was performed using the randomForest package in R. RPPA data for 152 TNBC patients in the TCGA dataset (TCPA: The Cancer Proteome Atlas) was split into training (80%) and test (20%) sets. The expression levels of 105 proteins (protein without missing data in the TCGA and whose expression was also evaluated in our RPPA) were scaled to have an average of 0 and standard deviation of 1, and were used to train a random forest model for TNBCtype-4 classification by optimizing the number of proteins randomly selected at each split, using 10-fold cross validation. The model with the highest accuracy was validated on the test set, and used to predict the classification of the mice tumors to the four TNBC subtypes. Hierarchical clustering of the RPPA data and partition clustering were performed and visualized using the gplots and Factoextra packages in R.

Statistical analysis

Data are presented as the median or as the mean ± standard error of the mean (s.e.m.), according to sample distributions. For two sided comparisons, we used unpaired Student's t test for data showing normal distributions and Wilcoxon test in other situations. For multiple comparisons, ANOVA test followed by Tukey test were used. ANOVA to analyse the RPPA outcomes was performed using the Partek Genomic Suite. P values are indicated in figures. The cumulative overall disease-free survival rates were calculated using the Kaplan-Meier method. $P < 0.05$ was considered significant.

References

1. Fantozzi A, Christofori G. Mouse models of breast cancer metastasis. Breast Cancer Res **2006**;8(4):212 doi 10.1186/bcr1530.
2. Park MK, Lee CH, Lee H. Mouse models of breast cancer in preclinical research. Lab Anim Res **2018**;34(4):160-5 doi 10.5625/lar.2018.34.4.160.
3. Christenson JL, Butterfield KT, Spoelstra NS, Norris JD, Josan JS, Pollock JA*, et al.* MMTV-PyMT and Derived Met-1 Mouse Mammary Tumor Cells as Models for Studying the Role of the Androgen Receptor in Triple-Negative Breast Cancer Progression. Horm Cancer-Us **2017**;8(2):69-77 doi 10.1007/s12672-017-0285-6.
4. Gerratana L, Basile D, Buono G, De Placido S, Giuliano M, Minichillo S*, et al.* Androgen receptor in triple negative breast cancer: A potential target for the targetless subtype. Cancer treatment reviews **2018**;68:102-10 doi 10.1016/j.ctrv.2018.06.005.
5. Lehmann BD, Jovanovic B, Chen X, Estrada MV, Johnson KN, Shyr Y*, et al.* Refinement of Triple-Negative Breast Cancer Molecular Subtypes: Implications for Neoadjuvant Chemotherapy Selection. PLoS One **2016**;11(6):e0157368 doi 10.1371/journal.pone.0157368.
6. Kohler BA, Sherman RL, Howlader N, Jemal A, Ryerson AB, Henry KA*, et al.* Annual Report to the Nation on the Status of Cancer, 1975-2011, Featuring Incidence of Breast Cancer Subtypes by Race/Ethnicity, Poverty, and State. J Natl Cancer Inst **2015**;107(6):djv048 doi 10.1093/jnci/djv048.
7. Garrido-Castro AC, Lin NU, Polyak K. Insights into Molecular Classifications of Triple-Negative Breast Cancer: Improving Patient Selection for Treatment. Cancer Discovery **2019**;9(2):176-98 doi 10.1158/2159-8290.Cd-18-1177.
8. Kriegsmann M, Endris V, Wolf T, Pfarr N, Stenzinger A, Loibl S*, et al.* Mutational profiles in triple-negative breast cancer defined by ultradeep multigene sequencing show high rates of PI3K pathway alterations and clinically relevant entity subgroup specific differences. Oncotarget **2014**;5(20):9952-65 doi DOI 10.18632/oncotarget.2481.

9. Solimini NL, Luo J, Elledge SJ. Non-oncogene addiction and the stress phenotype of cancer cells. Cell **2007**;130(6):986-8 doi 10.1016/j.cell.2007.09.007.

10. Lev S. Targeted therapy and drug resistance in triple-negative breast cancer: the EGFR axis. Biochem Soc T **2020**;48:657-65 doi 10.1042/Bst20191055.

11. Bianchini G, Balko JM, Mayer IA, Sanders ME, Gianni L. Triple-negative breast cancer: challenges and opportunities of a heterogeneous disease. Nat Rev Clin Oncol **2016**;13(11):674-90 doi 10.1038/nrclinonc.2016.66.

12. Jhan JR, Andrechek ER. Triple-negative breast cancer and the potential for targeted therapy. Pharmacogenomics **2017**;18(17):1595-609 doi 10.2217/pgs-2017-0117.

13. Matheson CJ, Backos DS, Reigan P. Targeting WEE1 Kinase in Cancer. Trends in pharmacological sciences **2016**;37(10):872-81 doi 10.1016/j.tips.2016.06.006.

14. Geenen JJJ, Schellens JHM. Molecular Pathways: Targeting the Protein Kinase Wee1 in Cancer. Clinical Cancer Research **2017**;23(16):4540-4 doi 10.1158/1078-0432.Ccr-17-0520.

15. Bridges KA, Hirai H, Buser CA, Brooks C, Liu H, Buchholz TA*, et al.* MK-1775, a novel Wee1 kinase inhibitor, radiosensitizes p53-defective human tumor cells. Clin Cancer Res **2011**;17(17):5638-48 doi 10.1158/1078-0432.CCR-11-0650.

16. Aarts M, Sharpe R, Garcia-Murillas I, Gevensleben H, Hurd MS, Shumway SD*, et al.* Forced Mitotic Entry of S-Phase Cells as a Therapeutic Strategy Induced by Inhibition of WEE1. Cancer Discovery **2012**;2(6):524-39 doi 10.1158/2159-8290.Cd-11-0320.

17. Zheng H, Shao F, Martin S, Xu X, Deng CX. WEE1 inhibition targets cell cycle checkpoints for triple negative breast cancers to overcome cisplatin resistance. Scientific reports **2017**;7:43517 doi 10.1038/srep43517.

18. Lewis CW, Jin Z, Macdonald D, Wei W, Qian XJ, Choi WS*, et al.* Prolonged mitotic arrest induced by Wee1 inhibition sensitizes breast cancer cells to paclitaxel. Oncotarget **2017**;8(43):73705-22 doi 10.18632/oncotarget.17848.

19. Jin J, Fang HH, Yang F, Ji WF, Guan N, Sun ZJ*, et al.* Combined Inhibition of ATR and WEE1 as a Novel Therapeutic Strategy in Triple-Negative Breast Cancer. Neoplasia **2018**;20(5):478-88 doi 10.1016/j.neo.2018.03.003.

20. Bukhari AB, Lewis CW, Pearce JJ, Luong D, Chan GK, Gamper AM. Inhibiting Wee1 and ATR kinases produces tumor-selective synthetic lethality and suppresses metastasis. Journal of Clinical Investigation **2019**;129(3):1329-44 doi 10.1172/Jci122622.

21. Liu JC, Granieri L, Shrestha M, Wang DY, Vorobieva I, Rubie EA*, et al.* Identification of CDC25 as a Common Therapeutic Target for Triple-Negative Breast Cancer. Cell reports **2018**;23(1):112-26 doi 10.1016/j.celrep.2018.03.039.

22. Fang Y, McGrail DJ, Sun CY, Labrie M, Chen XH, Zhang D*, et al.* Sequential Therapy with PARP and WEE1 Inhibitors Minimizes Toxicity while Maintaining Efficacy. Cancer Cell **2019**;35(6):851-+ doi 10.1016/j.ccell.2019.05.001.

23. Pfister SX, Markkanen E, Jiang YY, Sarkar S, Woodcock M, Orlando G*, et al.* Inhibiting WEE1 Selectively Kills Histone H3K36me3-Deficient Cancers by dNTP Starvation. Cancer Cell **2015**;28(5):557-68 doi 10.1016/j.ccell.2015.09.015.

24. Pai CC, Hsu KF, Durley SC, Keszthelyi A, Kearsey SE, Rallis C*, et al.* An essential role for dNTP homeostasis following CDK-induced replication stress. J Cell Sci **2019**;132(6) doi 10.1242/jcs.226969.

25. Mahajan K, Fang B, Koomen JM, Mahajan NP. H2B Tyr37 phosphorylation suppresses expression of replication-dependent core histone genes. Nat Struct Mol Biol **2012**;19(9):930-7 doi 10.1038/nsmb.2356.

26. Miles DM, Desdouets C, Geli V. Histone stress: an unexplored source of chromosomal instability in cancer? Curr Genet **2019**;65(5):1081-8 doi 10.1007/s00294-019-00967-x.

27. Fan YN, Arechederra M, Richelme S, Daian F, Novello C, Calderaro J*, et al.* A Phosphokinome-Based Screen Uncovers New Drug Synergies for Cancer Driven by Liver-Specific Gain of

Nononcogenic Receptor Tyrosine Kinases. Hepatology **2017**;66(5):1644-61 doi 10.1002/hep.29304.

28. Munoz B, Bolander FF, Jr. Prolactin regulation of mouse mammary tumor virus (MMTV) expression in normal mouse mammary epithelium. Mol Cell Endocrinol **1989**;62(1):23-9 doi 10.1016/0303-7207(89)90109-3.

29. Hamada N, Engelman RW, Tomita Y, Chen RF, Iwai H, Good RA*, et al.* Prolactin effects on the dietary regulation of mouse mammary tumor virus proviral DNA expression. Proc Natl Acad Sci U S A **1990**;87(17):6733-7 doi 10.1073/pnas.87.17.6733.

30. Niranjan B, Buluwela L, Yant J, Perusinghe N, Atherton A, Phippard D*, et al.* HGF/SF: a potent cytokine for mammary growth, morphogenesis and development. Development **1995**;121(9):2897-908.

31. Pepper MS, Soriano JV, Menoud PA, Sappino AP, Orci L, Montesano R. Modulation of hepatocyte growth factor and c-met in the rat mammary gland during pregnancy, lactation, and involution. Exp Cell Res **1995**;219(1):204-10 doi 10.1006/excr.1995.1220.

32. Henry MD, Triplett AA, Oh KB, Smith GH, Wagner KU. Parity-induced mammary epithelial cells facilitate tumorigenesis in MMTV-neu transgenic mice. Oncogene **2004**;23(41):6980-5.

33. Minuti G, Landi L. MET deregulation in breast cancer. Ann Transl Med **2015**;3(13):181 doi 10.3978/j.issn.2305-5839.2015.06.22.

34. Ho-Yen CM, Jones JL, Kermorgant S. The clinical and functional significance of c-Met in breast cancer: a review. Breast Cancer Res **2015**;17:52 doi 10.1186/s13058-015-0547-6.

35. Zagouri F, Bago-Horvath Z, Rossler F, Brandstetter A, Bartsch R, Papadimitriou CA*, et al.* High MET expression is an adverse prognostic factor in patients with triple-negative breast cancer. Br J Cancer **2013**;108(5):1100-5 doi 10.1038/bjc.2013.31.

36. Shimizu H, Nakayama KI. A 23 gene-based molecular prognostic score precisely predicts overall survival of breast cancer patients. Ebiomedicine **2019**;46:150-9 doi 10.1016/j.ebiom.2019.07.046.

37. Shattuck DL, Miller JK, Carraway KL, 3rd, Sweeney C. Met receptor contributes to trastuzumab resistance of Her2-overexpressing breast cancer cells. Cancer Res **2008**;68(5):1471-7.

38. Liu H, Murphy CJ, Karreth FA, Emdal KB, White FM, Elemento O*, et al.* Identifying and Targeting Sporadic Oncogenic Genetic Aberrations in Mouse Models of Triple-Negative Breast Cancer. Cancer Discov **2018**;8(3):354-69 doi 10.1158/2159-8290.CD-17-0679.

39. Verma N, Muller AK, Kothari C, Panayotopoulou E, Kedan A, Selitrennik M*, et al.* Targeting of PYK2 Synergizes with EGFR Antagonists in Basal-like TNBC and Circumvents HER3-Associated Resistance via the NEDD4-NDRG1 Axis. Cancer Research **2017**;77(1):86-99 doi 10.1158/0008-5472.Can-16-1797.

40. Ha DH, Min A, Kim S, Kim SH, Jang H, Kim YJ*, et al.* Antitumor effects of WEE1 inhibitor, AZD1775 alone or in combination with PARP inhibitor in triple negative breast cancer cells. Cancer Research **2018**;78(13) doi 10.1158/1538-7445.Am2018-2814.

41. Li Q, Saito TT, Martinez-Garcia M, Deshong AJ, Nadarajan S, Lawrence KS*, et al.* The tumor suppressor BRCA1-BARD1 complex localizes to the synaptonemal complex and regulates recombination under meiotic dysfunction in Caenorhabditis elegans. PLoS genetics **2018**;14(11):e1007701 doi 10.1371/journal.pgen.1007701.

42. Prigent C, Dimitrov S. Phosphorylation of serine 10 in histone H3, what for? Journal of Cell Science **2003**;116(18):3677-85 doi 10.1242/jcs.00735.

43. Castellano-Pozo M, Santos-Pereira JM, Rondon AG, Barroso S, Andujar E, Perez-Alegre M*, et al.* R loops are linked to histone H3 S10 phosphorylation and chromatin condensation. Mol Cell **2013**;52(4):583-90 doi 10.1016/j.molcel.2013.10.006.

44. Verma N, Vinik Y, Saroha A, Ulhas Nair N, Ruppin E, Mills G*, et al.* Synthetic lethal combination targeting BET uncovered intrinsic susceptibility of TNBC to ferroptosis. Science Advances, in press **2020**.

45. Holen I, Speirs V, Morrissey B, Blyth K. In vivo models in breast cancer research: progress, challenges and future directions. Dis Model Mech **2017**;10(4):359-71 doi 10.1242/dmm.028274.

46. Liang TJ, Reid AE, Xavier R, Cardiff RD, Wang TC. Transgenic expression of tpr-met oncogene leads to development of mammary hyperplasia and tumors. J Clin Invest **1996**;97(12):2872-7 doi 10.1172/JCI118744.

47. Graveel CR, DeGroot JD, Su Y, Koeman J, Dykema K, Leung S*, et al.* Met induces diverse mammary carcinomas in mice and is associated with human basal breast cancer. Proc Natl Acad Sci U S A **2009**;106(31):12909-14 doi 10.1073/pnas.0810403106.

48. Ponzo MG, Lesurf R, Petkiewicz S, O'Malley FP, Pinnaduwage D, Andrulis IL*, et al.* Met induces mammary tumors with diverse histologies and is associated with poor outcome and human basal breast cancer. Proc Natl Acad Sci U S A **2009**;106(31):12903-8 doi 10.1073/pnas.0810402106.

49. Liu S, Li S, Wang B, Liu W, Gagea M, Chen H*, et al.* Cooperative Effect of Oncogenic MET and PIK3CA in an HGF-Dominant Environment in Breast Cancer. Mol Cancer Ther **2019**;18(2):399-412 doi 10.1158/1535-7163.MCT-18-0710.

50. Kim YJ, Choi JS, Seo J, Song JY, Lee SE, Kwon MJ*, et al.* MET is a potential target for use in combination therapy with EGFR inhibition in triple-negative/basal-like breast cancer. Int J Cancer **2014**;134(10):2424-36 doi 10.1002/ijc.28566.

51. Comoglio PM, Trusolino L, Boccaccio C. Known and novel roles of the MET oncogene in cancer: a coherent approach to targeted therapy. Nature Reviews Cancer **2018**;18(6):341-58 doi 10.1038/s41568-018-0002-y.

52. Knudsen BS, Vande Woude G. Showering c-MET-dependent cancers with drugs. Curr Opin Genet Dev **2008**;18(1):87-96.

53. Linklater ES, Tovar EA, Essenburg CJ, Turner L, Madaj Z, Winn ME*, et al.* Targeting MET and EGFR crosstalk signaling in triple-negative breast cancers. Oncotarget **2016**;7(43):69903-15 doi 10.18632/oncotarget.12065.

54. Han Y, Chen MK, Wang HL, Hsu JL, Li CW, Chu YY*, et al.* Synergism of PARP inhibitor fluzoparib (HS10160) and MET inhibitor HS10241 in breast and ovarian cancer cells. Am J Cancer Res **2019**;9(3):608-18.

55. Chu YY, Yam C, Chen MK, Chan LC, Xiao M, Wei YK*, et al.* Blocking c-Met and EGFR reverses acquired resistance of PARP inhibitors in triple-negative breast cancer. Am J Cancer Res **2020**;10(2):648-61.

56. Kamalati T, Niranjan B, Yant J, Buluwela L. HGF/SF in mammary epithelial growth and morphogenesis: In vitro and in vivo models. J Mammary Gland Biol **1999**;4(1):69-77 doi Doi 10.1023/A:1018756620265.

57. Arechederra M, Daian F, Yim A, Bazai SK, Richelme S, Dono R*, et al.* Hypermethylation of gene body CpG islands predicts high dosage of functional oncogenes in liver cancer. Nat Commun **2018**;9(1):3164 doi 10.1038/s41467-018-05550-5.

58. Cassol F, Portal L, Richelme S, Dupont M, Boursier Y, Arechederra M*, et al.* Tracking Dynamics of Spontaneous Tumors in Mice Using Photon-Counting Computed Tomography. iScience **2019**;21:68-83 doi 10.1016/j.isci.2019.10.015.

59. Fan YN, Bazai SK, Daian F, Arechederra M, Richelme S, Temiz NA*, et al.* Evaluating the landscape of gene cooperativity with receptor tyrosine kinases in liver tumorigenesis using transposon-mediated mutagenesis. Journal of Hepatology **2019**;70(3):470-82 doi 10.1016/j.jhep.2018.11.027.

60. Peacock JD, Pridgeon MG, Tovar EA, Essenburg CJ, Bowman M, Madaj Z*, et al.* Genomic Status of MET Potentiates Sensitivity to MET and MEK Inhibition in NF1-Related Malignant Peripheral Nerve Sheath Tumors. Cancer Res **2018**;78(13):3672-87 doi 10.1158/0008-5472.CAN-17-3167.

61. Brunen D, Bernards R. Drug therapy: Exploiting synthetic lethality to improve cancer therapy. Nat Rev Clin Oncol **2017**;14(6):331-2 doi 10.1038/nrclinonc.2017.46.

62. Greider C, Chattopadhyay A, Parkhurst C, Yang E. BCL-x(L) and BCL2 delay Myc-induced cell cycle entry through elevation of p27 and inhibition of G1 cyclin-dependent kinases. Oncogene **2002**;21(51):7765-75 doi 10.1038/sj.onc.1205928.

63. Fan Y, Richelme S, Avazeri E, Audebert S, Helmbacher F, Dono R*, et al.* Tissue-Specific Gain of RTK Signalling Uncovers Selective Cell Vulnerability during Embryogenesis. PLoS genetics **2015**;11(9):e1005533 doi 10.1371/journal.pgen.1005533.

64. Genestine M, Caricati E, Fico A, Richelme S, Hassani H, Sunyach C*, et al.* Enhanced neuronal Met signalling levels in ALS mice delay disease onset. Cell Death Dis **2011**;2:e130.

65. Ianevski A, He L, Aittokallio T, Tang J. SynergyFinder: a web application for analyzing drug combination dose-response matrix data. Bioinformatics **2017**;33(15):2413-5 doi 10.1093/bioinformatics/btx162.

66. Furlan A, Roux B, Lamballe F, Conti F, Issaly N, Daian F*, et al.* Combined drug action of 2-phenylimidazo[2,1-b]benzothiazole derivatives on cancer cells according to their oncogenic molecular signatures. PLoS One **2012**;7(10):e46738 doi 10.1371/journal.pone.0046738.

67. Wagner KU, McAllister K, Ward T, Davis B, Wiseman R, Hennighausen L. Spatial and temporal expression of the Cre gene under the control of the MMTV-LTR in different lines of transgenic mice. Transgenic Res **2001**;10(6):545-53 doi Doi 10.1023/A:1013063514007.

Acknowledgments. We thank: all members of our labs for helpful discussions and comments; R. Dono and F. Helmbacher for extremely valuable feedback on the study; A. Furlan for initial work with *MMTV-R26^{Met}* mice; S. Richelme for *in vivo* bioluminescence imaging reported in Fig. 1B and for work on a first cohort of mice; E. Marechal for her contribution to the *MMTV-R26^{Met}* characterization; M. Buferne for *in vivo* bioluminescence imaging; the animal house platform for excellent help with mouse husbandry.

Funding. This research was supported by a grant from the Ministry of Foreign Affairs and International Development (MAEDI) and the Ministry of National Education, Higher Education and Research (MENESR) of France and by the Ministry of Science and Technology of Israel (Grant #3-14002) to F.M. and S.L. F.A. was supported by the Higher Education Commission (HEC) of Pakistan. U.A.K. was supported by the Rising Tide Foundation Cancer Research Postdoctoral Fellowship, the Dean Fellowship of the Faculty of Biology of the Weizmann Institute of Science (WIS), and the Postdoctoral Fellowship of the Swiss Society of Friends of the WIS. J-P.B. is a scholar of Institut Universitaire de France. V.G. is supported by the "Ligue Nationale Contre le Cancer" (Equipe Labellisée). The contribution of the Region Provence Alpes Côtes d'Azur and of the Aix-Marseille University to the IBDM animal facility and of the France-BioImaging/PICsL infrastructure (ANR-10-INBS-04-01) to the imaging facility are also acknowledged. The funders had no role in study design, data collection and analysis, decision to publish or preparation of the manuscript.

Author contributions

F.L.: designed and supervised studies, performed the majority of the experiments, data analysis, and interpretation; contributed to write the manuscript.

F.A.: performed the majority of the experiments under supervision of F.L., data analysis, and interpretation.

Y.V.: performed computational work with mouse and human TNBC databases, machine learning analyses, and interpretation; provided inputs on studies and on the manuscript.

O.C.: contributed to cell viability and biochemical studies; data processing.

F.D.: contributed to computational work with drug response data on cells, data analysis, and interpretation.

A.K.M.: performed histological analysis on *MMTV-R26*^{Met} samples, data analysis, and interpretation; provided input on the manuscript.

U.A.K.: performed histological analysis on *MMTV-R26*^{Met} samples, data analysis, and interpretation; provided input on the manuscript.

A.L.B.: performed FACS studies, data analysis, and interpretation.

E.J.: performed orthotopic studies and data analysis.

R.C.: performed orthotopic studies and data analysis.

C.C.: performed cell fractionation studies and data analysis.

E.C.J.: supervised and performed histological analysis on *MMTV-R26*^{Met} samples, data analysis, and interpretation; provided input on the manuscript.

G.B.M.: contributed to RPPA studies; provided input on the manuscript.

V.G.: provided input on studies and contributed to write the manuscript.

J.P.B.: provided input on studies and contributed to write the manuscript.

S.L.: designed and supervised studies on histological and RPPA analysis; provided input on studies; contributed to interpret data and to write the manuscript.

F.M.: designed and supervised the study, contributed to experimental work, analysed and interpreted data, ensured financial support, and wrote the manuscript.

Figures and Figure Legends

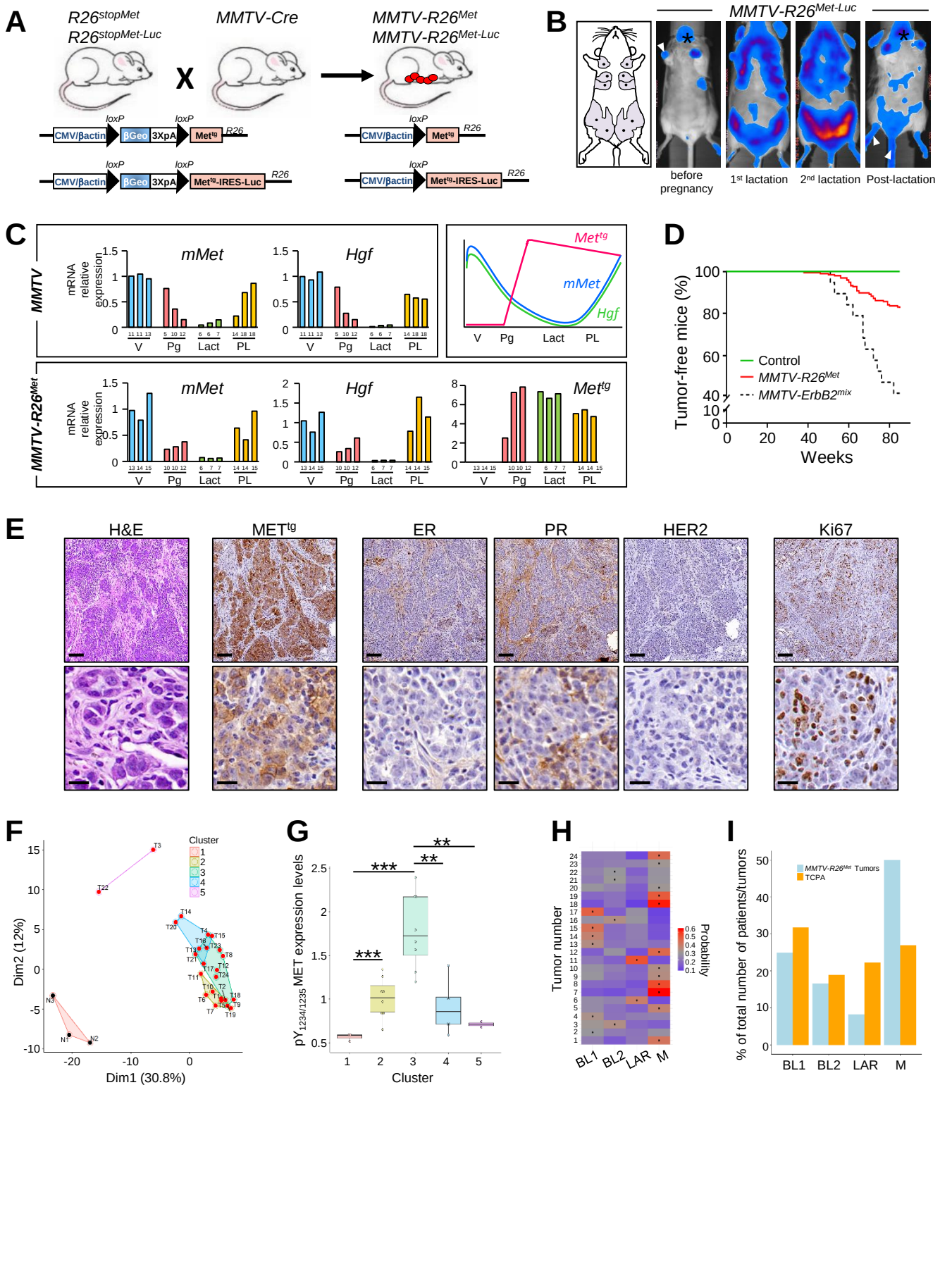
A
R26stopMet
R26stopMet-Luc
MMTV-Cre
MMTV-R26Met
MMTV-R26Met-Luc
X
loxP
CMV/βactin
βGeo
3XpA
Metfg
R26
Metfg-IRES-Luc
B
MMTV-R26Met-Luc
before pregnancy
1st lactation
2nd lactation
Post-lactation
C
MMTV
MMTV-R26Met
mRNA relative expression
mMet
Hgf
Metfg
V
Pg
Lact
PL
D
Tumor-free mice (%)
Weeks
Control
MMTV-R26Met
MMTV-ErbB2mix
E
H&E
METtg
ER
PR
HER2
Ki67
F
Cluster
Dim1 (30.8%)
Dim2 (12%)
G
pY1234/1235 MET expression levels
Cluster
H
Tumor number
Probability
BL1
BL2
LAR
M
I
% of total number of patients/tumors
MMTV-R26Met Tumors
TCPA

Figure 1

Figure 1. Increased expression of wild-type MET levels in the mouse mammary gland leads to Triple-Negative Breast Cancer formation. (A) Strategy used to enhance wild-type MET in the mammary gland of mice. The *R26*^{stopMet} mouse line, carrying the LacZ-stop cassette followed by chimeric *Met*^{tg}, was crossed with the *MMTV-Cre* mice, carrying the Cre recombinase under the control of the mouse mammary tumor virus *MMTV* promoter. After recombination, expression of the *Met*^{tg} is ensured by the removal of the LacZ-stop cassette (*MMTV-R26*^{Met} mice). The same strategy was used to generate transgenic mice carrying the LacZ-stop cassette followed by *Met*^{tg} and IRES-Luciferase before (*R26*$^{stopMet-Luc}$) and after (*MMTV-R26*$^{Met-Luc}$) Cre-mediated recombination. **(B)** Non-invasive *in vivo* bioluminescence imaging of *MMTV-R26*$^{Met-Luc}$ mice. Imaged mice were either not pregnant, under lactation (first or second lactation cycle), or in post-lactation phase. Although mainly detected in the mammary glands, low luciferase expression was also observed in the salivary gland (asterisk), in the skin of the paws and tail (white arrowhead), which is due to partial leakage of the *MMTV-Cre* line, as previously reported (67). The five pairs of the mouse mammary glands are depicted on the scheme in the left. **(C)** RT-qPCR analyses showing transcript levels of the endogenous mouse *Met* (*mMet*), *Hgf*, and the *Met*^{tg}, in mammary glands of either *MMTV* (upper left panel) or *MMTV-R26*^{Met} (lower panel) mice. Mammary fat pads of three different mice were used for each stage. The age of each mouse is indicated (for virgin animals (V): in weeks; for the other stages: pregnancy (Pg), lactation (Lact), and post-lactation (PL): in days). The scheme on the top right illustrates the dynamic expression of the various transcripts. Note that during lactation, the expression levels of the endogenous *Met* and *Hgf* transcripts are very low, whereas expression of the *Met*^{tg} is maintained. **(D)** Kaplan-Meier analysis of mammary gland tumor incidence in *MMTV-R26*^{Met}, control (*R26*^{STOPMet}), and *MMTV-ErbB2* mice generated in the same mixed (C57/129, 50%/50%) genetic background (*MMTV-ErbB2*^{mix}). **(E)** Representative histopathological and immunohistological analysis of *MMTV-R26*^{Met} tumors using hematoxylin/eosin (H&E), anti-human MET staining to detect expression of the MET transgene (MET^{tg}), anti-Ki67 to assess the proliferative index. Expression of the estrogen- (ER), progesterone-(PR), and ErbB2 receptors (HER2) were also analyzed. Scale bar: top panel: 100µm, bottom panel: 20µm. **(F)** K-

means clustering of the tumors (red dots, n=24) and normal samples (black dots, n=3). Clustering was done with all proteins present in the RPPA, and using k=5 clusters. Clustering is shown in Principal Component Analysis (PCA) plot using the two highest principal components. **(G)** Clusters defined in (F) are characterized by different MET phosphorylation status. **(H)** Heatmap depicting the probability that each tumor belongs to a specific subtype. The black dots indicate the type with the highest probability for each tumor. BL1: basal-like-1; BL2: basal-like-2; LAR: luminal androgen receptor; M: mesenchymal. **(I)** Histogram reporting enrichment of the tumors compared to the TCPA. Note that, even though all subtypes are represented, *MMTV-R26*^{Met} tumors are more enriched for the mesenchymal (M) subtype.

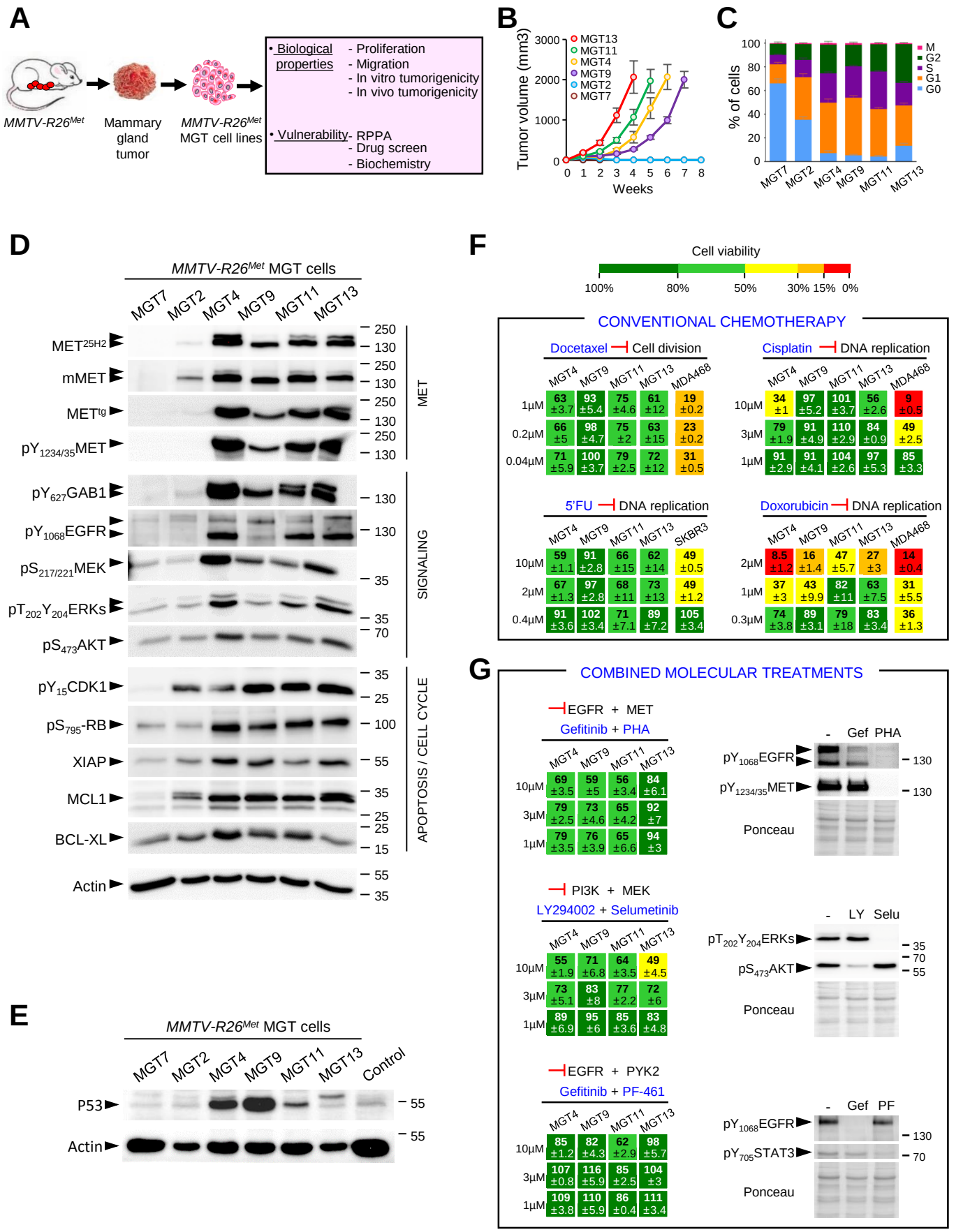
A
MMTV-R26Met
Mammary gland tumor
MMTV-R26Met MGT cell lines
• Biological properties
- Proliferation
- Migration
- In vitro tumorigenicity
- In vivo tumorigenicity
• Vulnerability
- RPPA
- Drug screen
- Biochemistry
B
Tumor volume (mm3)
Weeks
MGT13
MGT11
MGT4
MGT9
MGT2
MGT7
C
% of cells
M
G2
S
G1
G0
MGT7
MGT2
MGT4
MGT9
MGT11
MGT13
D
MMTV-R26Met MGT cells
MET25H2
mMET
METtg
pY1234/35MET
pY627GAB1
pY1068EGFR
pS217/221MEK
pT202Y204ERKs
pS473AKT
pY15CDK1
pS795-RB
XIAP
MCL1
BCL-XL
Actin
MET
SIGNALING
APOPTOSIS / CELL CYCLE
E
MMTV-R26Met MGT cells
Control
P53
Actin
F
Cell viability
100%
80%
50%
30%
15%
0%
CONVENTIONAL CHEMOTHERAPY
Docetaxel — Cell division
Cisplatin — DNA replication
5'FU — DNA replication
Doxorubicin — DNA replication
G
COMBINED MOLECULAR TREATMENTS
EGFR + MET
Gefitinib + PHA
Gef
PHA
Ponceau
PI3K + MEK
LY294002 + Selumetinib
LY
Selu
EGFR + PYK2
Gefitinib + PF-461
PF
pY705STAT3

Figure 2

Figure 2. Cells derived from *MMTV-R26^{Met}* mammary gland tumors recapitulate resistance to drugs used in conventional chemotherapies and to combined molecular treatments. (A) *MMTV-R26^{Met}* mammary gland tumors (MGT) were used to generate *MMTV-R26^{Met}* MGT cell lines, which were then utilized for assessing various biological properties and vulnerability to drugs. **(B)** *In vivo* tumorigenic properties of the *MMTV-R26^{Met}* cell lines. Xenografts studies were performed by subcutaneous injection of cells in the flank of nude mice (n=4-5, injected bilaterally). Evolution of the tumor volume shows that MGT4, MGT9, MGT11, and MGT13 are highly tumorigenic cell lines, whereas the MGT2 and MGT7 cells do not form tumors. **(C)** Histogram showing the percentage of cells from each cell line in each phase of the cell cycle as determined by flow cytometry using propidium iodide and Ki67 staining. Three independent experiments were performed. Statistical analyses are shown in Table S9. **(D)** Western blot analysis of total protein extracts from *MMTV-R26^{Met}* MGT cells. Actin and Ponceau S stainings were used as loading controls in all studies. **(E)** Western blot analysis of p53 expression levels in *MMTV-R26^{Met}* MGT cell lines compared to normal mammary epithelial cells (control). **(F)** Cell viability of *MMTV-R26^{Met}* MGT cells exposed to drugs conventionally used in chemotherapy. Human TNBC cell lines (MDA-MB-468 and SKBR3) were used as positive controls. Percentage of cell viability in presence of drugs compared to controls (untreated cells) is indicated. Values are expressed as the mean ± s.e.m. Percentages are reported using a color code (from green to red; the scale is shown on the top and is used as a reference in all studies). **(G)** Dose-response effects of drug used in combined treatments on the viability of *MMTV-R26^{Met}* MGT cells. Western blots depict the effect of each drug on its specific target. Note loss of EGFR phosphorylation in cells treated with PHA-665752, the MET inhibitor. 5'FU: 5-fluorouracil; Gef: gefitinib; LY: LY294002; PF: PF-461; PHA: PHA-665752; Selu: selumetinib.

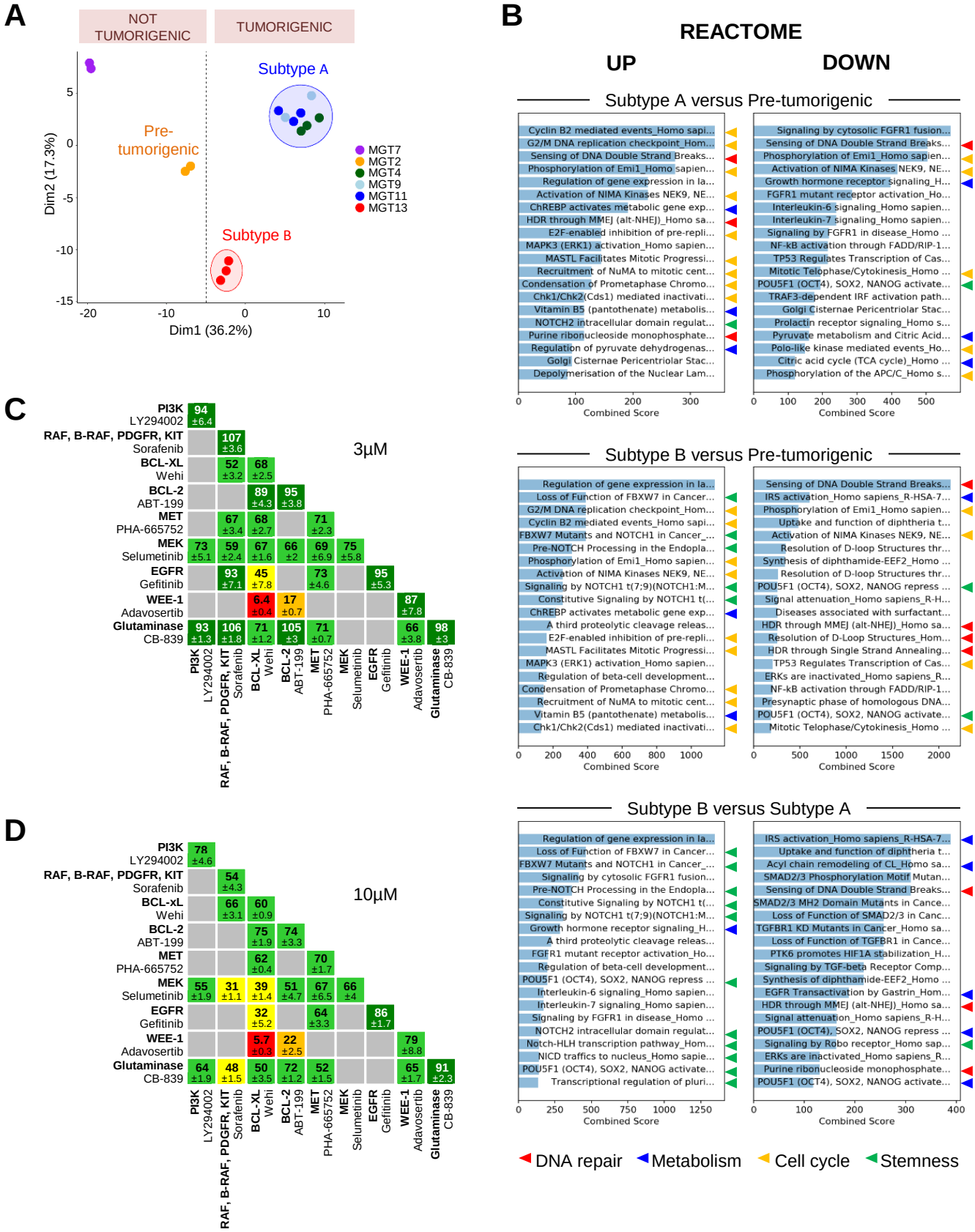
A
NOT TUMORIGENIC
TUMORIGENIC
Subtype A
Pre-tumorigenic
Subtype B
MGT7
MGT2
MGT4
MGT9
MGT11
MGT13
Dim2 (17.3%)
Dim1 (36.2%)
B
REACTOME
UP
DOWN
Subtype A versus Pre-tumorigenic
Subtype B versus Pre-tumorigenic
Subtype B versus Subtype A
Combined Score
C
3μM
PI3K LY294002
RAF, B-RAF, PDGFR, KIT Sorafenib
BCL-XL Wehi
BCL-2 ABT-199
MET PHA-665752
MEK Selumetinib
EGFR Gefitinib
WEE-1 Adavosertib
Glutaminase CB-839
D
10μM
DNA repair
Metabolism
Cell cycle
Stemness

Figure 3

Figure 3. Proteomic analysis highlighted signaling changes in *MMTV-R26^{Met}* tumors, leading to the identification of a new potent drug combination for TNBC cells. (A) Principal Component Analysis of the *MMTV-R26^{Met}* MGT cell lines, using Reverse Phase Protein Array (RPPA) data. The 2 non-tumorigenic cell lines are well separated from each other, with MGT2 that we named "pre-tumorigenic" cells. Both non-tumorigenic cells are distinct from the two tumorigenic cell clusters, designated as "subtype A" (MGT4, MGT9, MGT11) and "subtype B" (MGT13). **(B)** Proteomic profiles of cells belonging to the different clusters (shown in A) were compared to identify enrichments by applying the Enrichr software. Histograms report the enriched cell signaling pathways, using the Reactome database, ordered according to the combined score. The 20 top ranked enrichments are highlighted. Note that the majority of the changes are related to signals (indicated by arrowheads) involved in DNA repair (red), metabolism (blue), cell cycle regulation (yellow), and stemness (green) (indicated by colored arrowheads). **(C, D)** Representation of the drug screen outcomes performed on the MGT4 cell line, highlighting single and combined treatments tested. Drugs were used at a concentration of 3µM **(C)** and 10µM **(D)**. Numbers indicate the percentage of viable cells in the presence of drugs compared to controls (untreated cells), and labelled by the green-to-red color code. Values are expressed as the mean ± s.e.m. Grey squares correspond to untested drug effects. Note that targeting BCL-XL (with Wehi) and WEE1 (with Adavosertib) is highly deleterious (red color) for *MMTV-R26^{Met}* MGT4 cells compared to other drugs exhibiting no or minimal effects (green, yellow, orange).

A

MGT4

A11 ⊣ BCL-XL

	⊣ WEE1 Adav	-	WEE1 Adav
10µM	3.4 ±0.1	98 ±3	19 ±1
3µM	6.2 ±0.3	104 ±4	23 ±1.3
1µM	16 ±1	104 ±3.4	31 ±2

Drug (µM)		A1155463 0	0,3	1	3	10
Adav	0	100	107	100	96	94
	0,3	68	65	63	57	55
	1	26	14	10	9,1	7,1
	3	14	7,2	3,7	3,3	2,4
	10	7,8	2,6	2,4	2	1,4

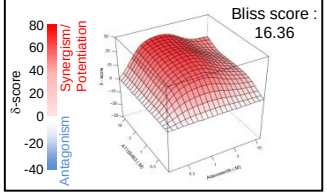

MGT9

A11 ⊣ BCL-XL

	⊣ WEE1 Adav	-	WEE1 Adav
10µM	11 ±1	62 ±2.5	62 ±0.4
3µM	18 ±0.5	76 ±4.1	74 ±0.3
1µM	31 ±0.1	81 ±0.8	74 ±0.1

Drug (µM)		A1155463 0	0,3	1	3	10
Adav	0	100	76	81	76	62
	0,3	88	66	66	63	52
	1	78	45	31	31	30
	3	72	28	18	18	15
	10	62	13	12	12	11

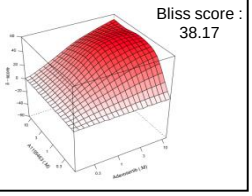

MGT11

A11 ⊣ BCL-XL

	⊣ WEE1 Adav	-	WEE1 Adav
10µM	3.1 ±0.1	66 ±3.5	81 ±3.1
3µM	5.6 ±0.4	72 ±4	78 ±5
1µM	25 ±0.5	67 ±1.5	80 ±8

Drug (µM)		A1155463 0	0,3	1	3	10
Adav	0	100	77	82	88	70
	0,3	94	60	66	61	71
	1	78	25	19	15	16
	3	57	12	7,7	6,8	8,2
	10	33	5,5	5,6	5,2	5,9

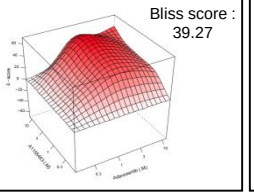

MGT13

A11 ⊣ BCL-XL

	⊣ WEE1 Adav	-	WEE1 Adav
10µM	2 ±0.1	114 ±4.1	27 ±0.1
3µM	5.9 ±0.1	119 ±8.2	44 ±0.6
1µM	12 ±0.4	114 ±8.3	52 ±0.2

Drug (µM)		A1155463 0	0,3	1	3	10
Adav	0	100	97	102	96	97
	0,3	56	29	27	24	15
	1	48	22	17	13	6,6
	3	36	12	9,3	6,2	4
	10	24	9,1	5,4	4,4	3,4

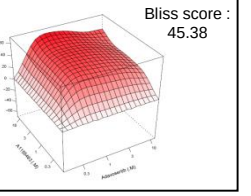

B

A11 ⊣ BCL-XL

		⊣ WEE1 Adav	-	WEE1 Adav
MGT2	10µM	40 ±1.4	101 ±3.4	70 ±1.3
	3µM	51 ±0.5	115 ±3.9	81 ±2.5
MGT7	10µM	78 ±1.4	89 ±2.6	87 ±3.8
	3µM	87 ±1.8	102 ±4.1	93 ±6.5

C

A11 ⊣ BCL-XL

		⊣ WEE1 Adav	-	WEE1 Adav
human TNBC	BT-549	9.6 ±0.3	74 ±2.9	24 ±0.3
	MDA-MB-231	12 ±1.1	71 ±0.2	67 ±1.7
	MDA-MB-468	9.6 ±3.3	51 ±2.4	16 ±1.5
	SUM159	1.9 ±0.4	57 ±1.6	11 ±0.1
	HCC-1937	2.8 ±0.2	26 ±1.1	12 ±0.9
	Hs578t	8.1 ±0.9	38 ±0.6	22 ±0.5

D

A11 ⊣ BCL-XL

		⊣ WEE1 Adav	-	WEE1 Adav
human non-TNBC	MCF-7	94 ±1.4	100 ±1.5	92 ±8.4
	MCF-7/HER2	23 ±3	87 ±8	36 ±1.1
	BT-474	52 ±4.1	77 ±2.6	59 ±3.3
	SK-BR-3	8.5 ±0.7	54 ±1.2	7.8 ±0.3

E

	MGT4							MGT9							MGT11							MGT13						
Cisp	-	-	-	-	-	+	+	-	-	-	-	-	+	+	-	-	-	-	-	+	+	-	-	-	-	-	+	+
Olap	-	-	-	+	+	-	-	-	-	-	+	+	-	-	-	-	-	+	+	-	-	-	-	-	+	+	-	-
AZD	-	+	+	-	-	-	-	-	+	+	-	-	-	-	-	+	+	-	-	-	-	-	+	+	-	-	-	-
Adav	+	-	+	-	+	-	+	+	-	+	-	+	-	+	+	-	+	-	+	-	+	+	-	+	-	+	-	+
10µM	24 ±4.1	38 ±0.4	26 ±0.4	89 ±3.6	33 ±1	35 ±1	15 ±0.3	79 ±3	71 ±1.1	53 ±3.1	84 ±2.1	80 ±1	85 ±3	55 ±3.5	72 ±4.4	85 ±0.2	56 ±2	95 ±0.8	55 ±1	101 ±3.7	47 ±1.6	28 ±1.6	33 ±1.7	23 ±1.3	76 ±3.4	22 ±0.7	56 ±2.5	17 ±1.3
3µM	23 ±3	52 ±2.6	21 ±0.5	95 ±3.8	27 ±1.2	79 ±2	15 ±0.5	82 ±1.8	88 ±6.3	66 ±4.2	91 ±2.2	78 ±0.6	95 ±5.8	78 ±1.6	75 ±1.8	101 ±1.4	65 ±2.6	93 ±1.5	63 ±0.9	109 ±2.8	77 ±0.6	41 ±2.9	51 ±3	35 ±1.3	90 ±0.6	36 ±0.3	84 ±0.9	38 ±2.6
1µM	28 ±1.5	90 ±4.6	24 ±0.1	99 ±5.6	28 ±1	91 ±2.1	22 ±1.4	84 ±3.6	105 ±6.4	78 ±3.1	94 ±2	82 ±1	94 ±5.6	78 ±1.6	92 ±7.8	106 ±1.2	79 ±2.5	94 ±1	77 ±1.2	103 ±2.6	101 ±2.2	47 ±1.8	74 ±3.2	40 ±0.6	94 ±4	47 ±0.8	97 ±5.3	47 ±2.3

F

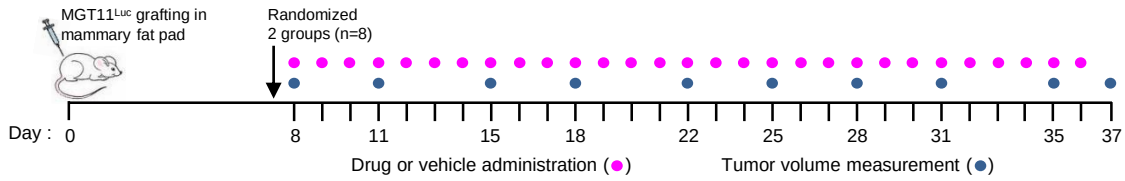

G

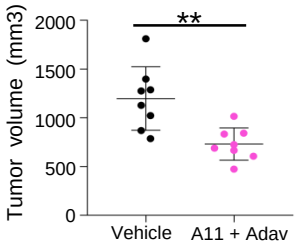

H

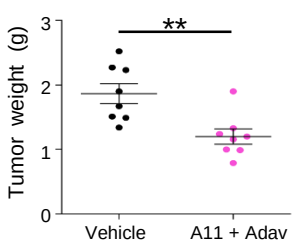

I

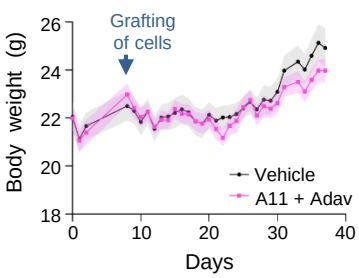

Figure 4

Figure 4. Combined inhibition of BCL-XL and WEE1 is deleterious for all *MMTV-R26^{Met}* MGT and human TNBC cell lines tested. (A) Dose-response effects of A1155463 (A11, targeting BCL-XL) alone or in combination with Adavosertib (Adav, targeting WEE1) on the viability of the four tumorigenic *MMTV-R26^{Met}* MGT cell lines. Combined drug effects are reported on the left of the top panel. Detailed matrix (middle panel) and Loewe plots (lower panel) highlight the drug synergism. **(B)** Cell viability assay performed on the non-tumorigenic MGT2 and MGT7 cell lines highlights the lack of *in vitro* toxic effect of A1155463+Adavosertib drug combination. **(C, D)** Cell viability in response of A1155463 (1µM) and Adavosertib (3µM) in a panel of human TNBC **(C)** and human non-TNBC breast cancer **(D)** cell lines. In all figures, cell viability is presented as percentage of control (untreated cells) and labelled by the green (high) to-red (low) color code. In A-D, at least three independent experiments were performed. **(E)** Dose-response effects on the viability of *MMTV-R26^{Met}* MGT cells treated with single or combined drugs as indicated. **(F-I)** *In vivo* effects of A1155463+Adavosertib treatment in orthotopic tumors. **(F)** Orthotopic injection of MGT11^{Luc} cells in the mammary fat pad of NSG mice, drug administration, and tumor volume measurement were performed as illustrated. Tumor volume **(G)** and tumor weight **(H)** measured at the end point of the experiment (day 37; n=8 mice per group). **(I)** Graph reporting the evolution of the body weight of mice during the whole procedure. Body weight was measured every day, before drug administration. No significant changes were observed, indicating that the dose of drugs used *in vivo* were not toxic. A11: A1155463 (BCL-XL inhibitor); Adav: Adavosertib (WEE1 inhibitor); AZD: AZD6738 (ATR inhibitor); Cisp: cisplatin; Olap: Olaparib (PARP inhibitor). Values are expressed as the mean ± s.e.m. ** $P < 0.01$.

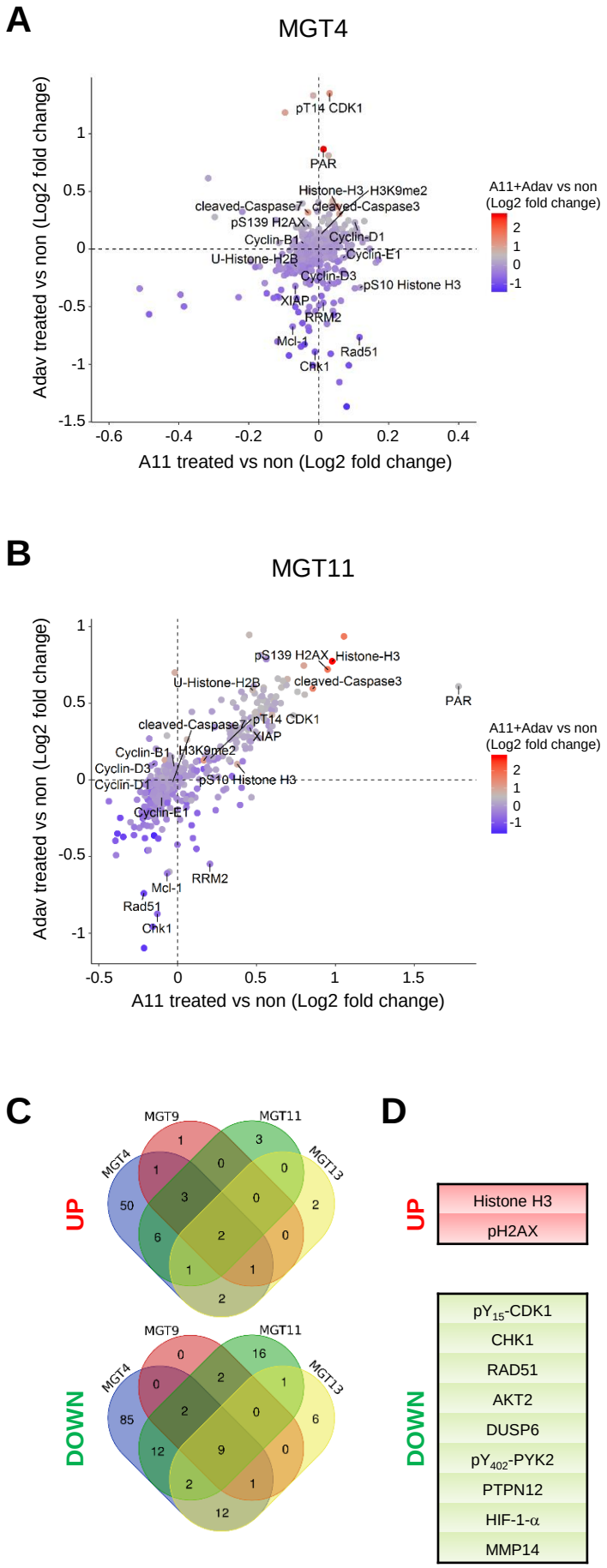
A
MGT4
Adav treated vs non (Log2 fold change)
A11 treated vs non (Log2 fold change)
pT14 CDK1
PAR
Histone-H3
H3K9me2
cleaved-Caspase7
cleaved-Caspase3
pS139 H2AX
Cyclin-B1
Cyclin-D1
Cyclin-E1
U-Histone-H2B
Cyclin-D3
pS10 Histone H3
XIAP
RRM2
Mcl-1
Rad51
Chk1
A11+Adav vs non
(Log2 fold change)
B
MGT11
C
MGT9
MGT11
MGT4
MGT13
UP
DOWN
D
Histone H3
pH2AX
pY15-CDK1
CHK1
RAD51
AKT2
DUSP6
pY402-PYK2
PTPN12
HIF-1-α
MMP14

Figure 5

Figure 5. BCL-XL and WEE1 targeting leads to perturbation of several signals, including epigenetic, DNA damage/repair, apoptosis, and cell cycle regulators. (A, B) Graph showing the fold change (Log_2) of protein phosphorylation or expression in MGT4 **(A)** and MGT11 **(B)** cells between: A1155463 (A11) versus untreated (on the x-axis), Adavosertib (Adav) versus untreated (on the y-axis), and the combination versus untreated (colors of the dots). Changes related to epigenetics (HistoneH3, H3K9me2, phosphoS$_{10}$HistoneH3, U-HistoneH2B, RRM2) DNA damage and repair (γH2AX, Rad51, PAR), apoptosis (cleaved Caspase7, cleaved Caspase3), and cell cycle (CHK1, CDK1, cyclins) are indicated. **(C, D)** Signaling changes occurring in the four *MMTV-R26^{Met}* MGT cell lines when treated with the drug combination (A1155463+Adavosertib). **(C)** Venn diagram representing overlapping changes in protein expression and/or phosphorylation levels (up or down) from intersection of the four *MMTV-R26^{Met}* MGT cell lines. A total of 2 upregulated and 9 downregulated overlapping signals were identified in all four analyzed cell lines. The various colored regions represent each *MMTV-R26^{Met}* MGT cell line as indicated. **(D)** List of the common modified signals in all *MMTV-R26^{Met}* MGT cell lines.

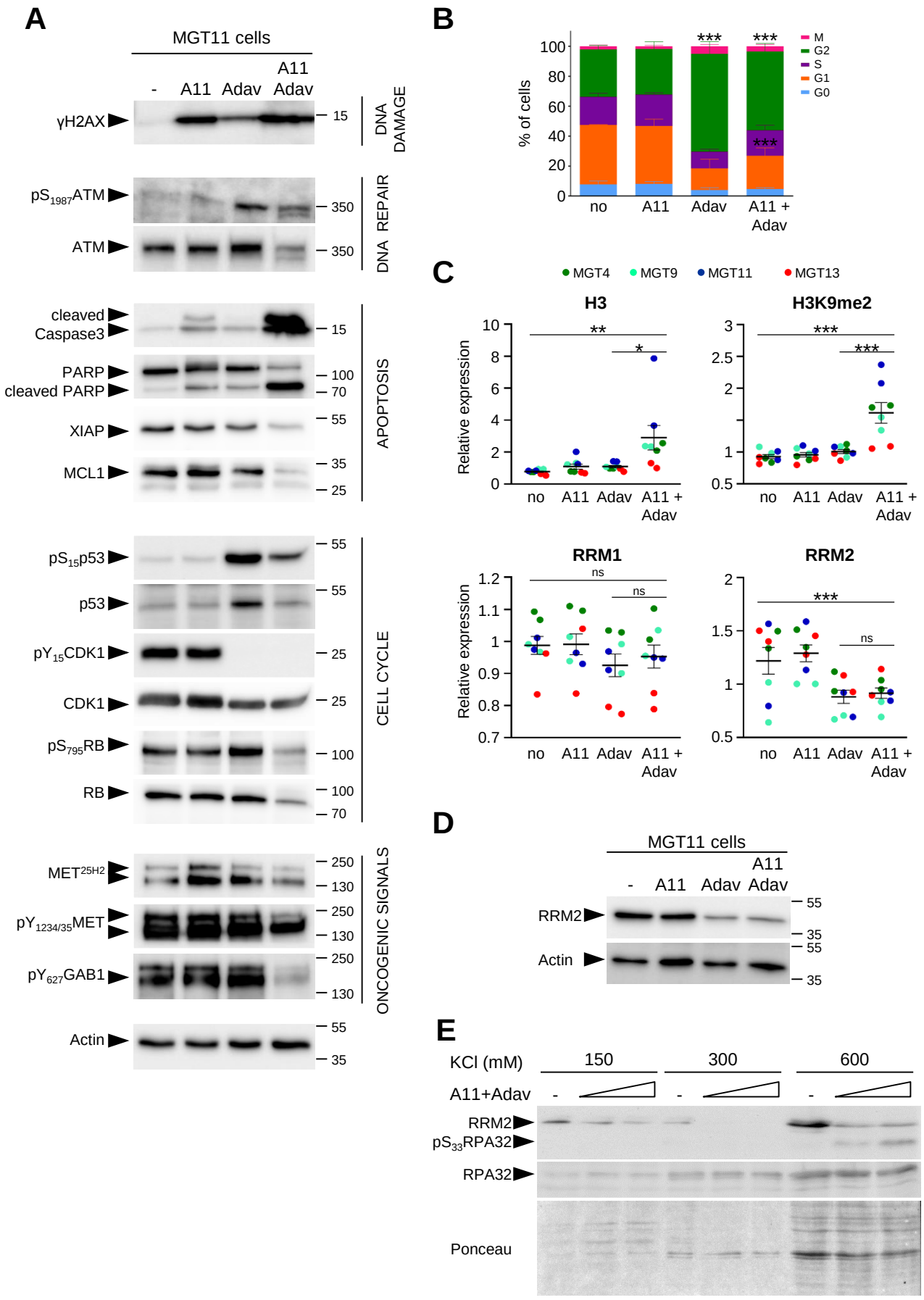
A
MGT11 cells
-
A11
Adav
A11 Adav
γH2AX
15
DNA DAMAGE
pS1987ATM
350
ATM
350
DNA REPAIR
cleaved Caspase3
15
PARP
100
cleaved PARP
70
XIAP
55
MCL1
35
25
APOPTOSIS
pS15p53
55
p53
55
pY15CDK1
25
CDK1
25
pS795RB
100
RB
100
70
CELL CYCLE
MET25H2
250
130
pY1234/35MET
250
130
pY627GAB1
250
130
ONCOGENIC SIGNALS
Actin
55
35
B
% of cells
100
80
60
40
20
0
***
***
***
M
G2
S
G1
G0
no
A11
Adav
A11 + Adav
C
MGT4
MGT9
MGT11
MGT13
H3
H3K9me2
RRM1
RRM2
Relative expression
**
*
***
***
ns
ns
***
ns
no
A11
Adav
A11 + Adav
D
MGT11 cells
-
A11
Adav
A11 Adav
RRM2
55
35
Actin
55
35
E
KCl (mM)
150
300
600
A11+Adav
-
-
-
RRM2
pS33RPA32
RPA32
Ponceau

Figure 6

Figure 6. BCL-XL targeting exacerbates WEE1 requirement in TNBC cells. (A) Western blots showing the effects of A1155463 (1µM), Adavosertib (3 µM), and combined treatment on the indicated signals in the MGT11 cells, 12hrs after treatment. **(B)** Graph reporting the distribution of cells treated with the indicated drugs (for 12hrs), compared to untreated cells (no), in each phase of the cell cycle as determined by flow cytometry using PI and Ki67 staining. **(C)** Graphs reporting changes by RPPA in levels of Histone H3, H3K9me2, RRM1, and RRM2 in MGT cells exposed to A1155463, Adavosertib, or in combination. Distinct MGT cell lines are indicated in colors. **(D)** Western blots showing RRM2 downregulation in MGT1 cells treated with Adavosertib alone or in combination with A1155463. **(E)** Western blot showing downregulation of RRM2 and increase of pS_{33}RPA32 levels in the chromatin fraction (corresponding to the 600mM KCl) of cells co-treated with WEE1+BCL-XL (A11+Adav). Cells were treated with A1155463 (0.3µM) plus Adavosertib (1µM or 3µM). Three independent experiments were performed. Values are expressed as the mean ± s.e.m. *** P <0.001. All statistical analyses are reported in Table S13. A11: A1155463; Adav: Adavosertib.

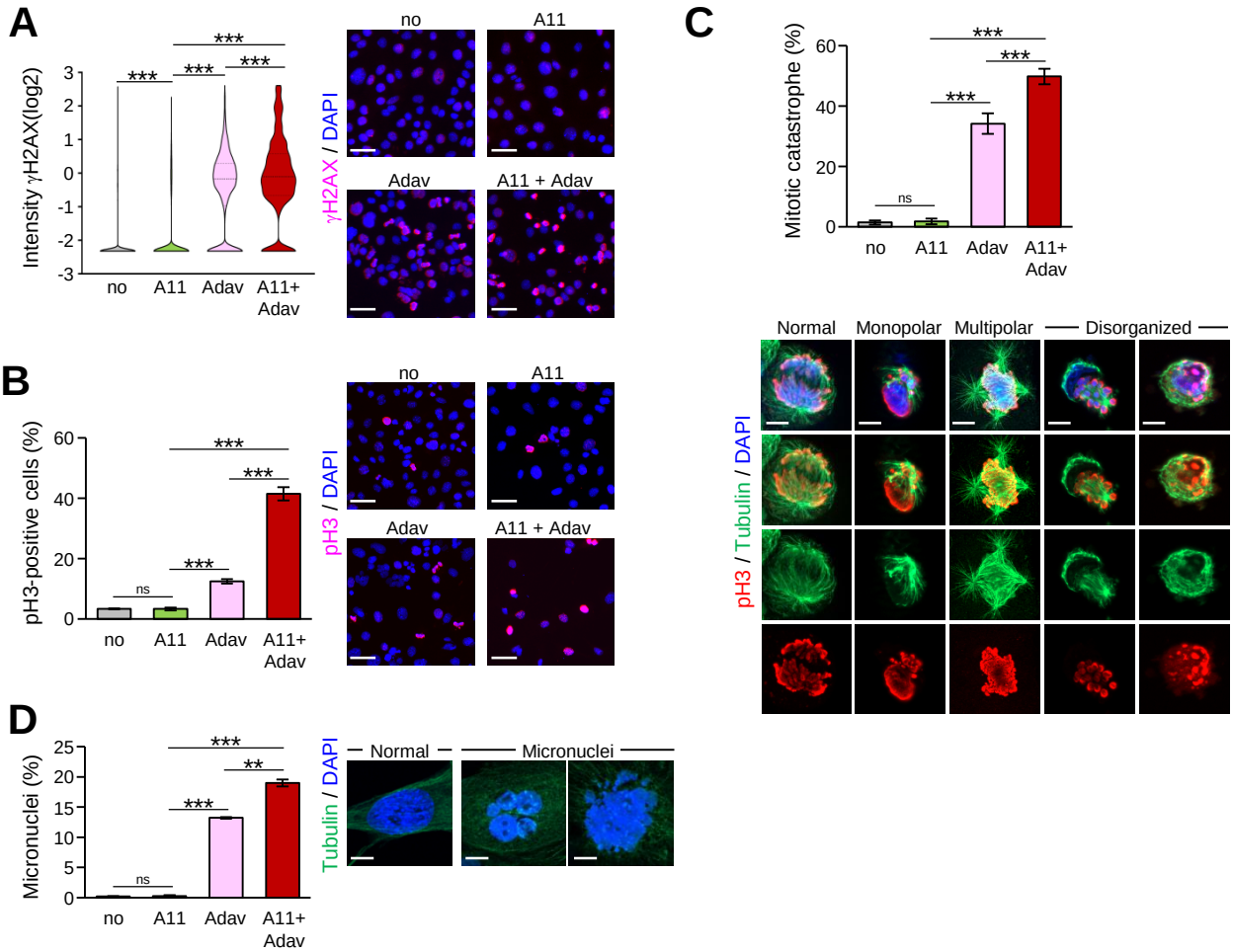
A
Intensity γH2AX(log2)
no
A11
Adav
A11+ Adav
γH2AX / DAPI
B
pH3-positive cells (%)
pH3 / DAPI
C
Mitotic catastrophe (%)
ns
Normal
Monopolar
Multipolar
Disorganized
pH3 / Tubulin / DAPI
D
Micronuclei (%)
Tubulin / DAPI
Micronuclei

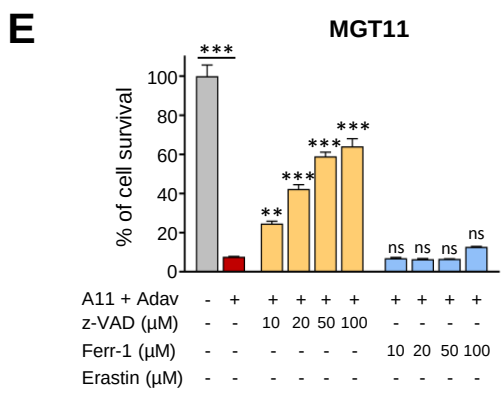
E
MGT11
% of cell survival
A11 + Adav
z-VAD (μM)
Ferr-1 (μM)
Erastin (μM)

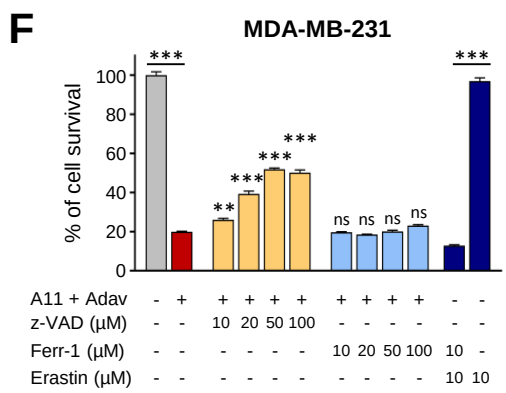
F
MDA-MB-231
% of cell survival
A11 + Adav
z-VAD (μM)
Ferr-1 (μM)
Erastin (μM)

Figure 7

Figure 7. Combined BCL-XL and WEE1 inhibition leads to mitotic catastrophe and apoptosis. Cells untreated or treated for the indicated times with A1155463 (0.3µM), Adavosertib (3µM), or in combination, were immunostained with the indicated antibodies. DAPI was used to counterstain the nuclear DNA. **(A)** MGT11 cells treated for 12hrs with the drugs were immunostained with anti- γH2AX antibodies. Left: the number of γH2AX-positive cells according to the intensity of staining is represented in the violin plot (Log_2). Right: representative images of γH2AX immunostaining. Scale bar: 50µm. Four independent experiments were performed. **(B, C)** MGT11 cells treated for 16hrs with the drugs were stained with anti-pH3 (red) and α-Tubulin (microtubules, green) antibodies. **(B)** Left: percentage of cells in mitosis (pH3-positive cells) versus total number of cells. Right: representative images of pH3 immunostaining. Scale bar: 50µm. **(C)** Quantifications (top) and examples (bottom) of cells harboring either typical mitotic phenotypes (normal) or mitotic catastrophe (monopolar, multipolar, or disorganized spindle) revealed by anti-pH3/α-Tubulin immunostaining. To calculate the percentage of cells harboring mitotic catastrophe, we considered cells in metaphase and anaphase among the pH3-positive cells. Scale bar: 5µm for multipolar spindle, 10µm for normal monopolar and disorganized spindle images. Three independent experiments were performed. **(D)** MGT11 cells were treated for 24hrs with the indicated drugs. Nuclear DNA was counterstained with DAPI. Percentage of cells with micronuclei versus the total number of cells (left) and representative images (right) are shown. Scale bar: 10µm. Three independent experiments were performed. **(E, F)** The pan-caspase inhibitor z-VAD-FMK rescues from cell death induced by the combination of A1155463 and Adavosertib. *MMTV-R26^{Met}* MGT11 **(E)** and MDA-MB-231 **(F)** cells were pretreated with either the apoptosis (z-VAD: z-VAD-FMK) or the ferroptosis (Ferr-1: Ferrostatin-1) inhibitor at the indicated doses, for 1hr and then for additional 24hrs in the absence or presence of A1155463 (A11, 0.3µM) + Adavosertib (Adav, 3µM). Histograms represent the percentage of cell viability in presence of drugs compared to controls (untreated cells). Statistics refer to cell viability obtained in presence of the apoptosis or ferroptosis inhibitors compared to A1155463+Adavosertib alone. The efficiency of Ferrostatin-1 was assessed in presence of Erastin, a ferroptosis inducer. Three independent

experiments were performed. Data are expressed as means ± s.e.m. ns $P>0.05$; ** $P<0.01$; *** $P<0.001$.